applied sciences

MDPI

Article

Orbital-Based Automatic Multi-Layer Multi-Pass Welding Equipment for Small Assembly Plates

Yang Cai [1], Gongzhi Yu [1,*,†], Jikun Yu [2,*,†] and Yayue Ji [1]

[1] School of Navigation and Marine Engineering, Dalian Ocean University, Dalian 116023, China; 15142870587@163.com (Y.C.); 15642812258@163.com (Y.J.)
[2] School of Applied Technology, Dalian Ocean University, Dalian 116300, China
* Correspondence: 19741166357@163.com (G.Y.); yujikun@dlou.edu.cn (J.Y.)
† These authors contributed equally to this work.

Abstract: To address the technical challenges, production quality issues, and inefficiencies caused by the heavy reliance on traditional manual processing of small assembly plates in the shipbuilding industry, this paper presents the design and analysis of a track-based automatic welding device. This equipment provides a solution for achieving batch and continuous welding in the field of automatic welding technology. The design section includes the mechanical design of the equipment's core mechanisms, the design of the operating systems, the development of visual scanning strategies under working conditions, and the formulation of multi-layer and multi-pass welding processes. The analysis section comprises the static analysis of the equipment's mechanical structure, kinematic analysis of the robotic arm, and inspection analysis of the device. Compared with manual welding, multi-layer and multi-pass welding experiments conducted using the equipment demonstrated stabilized welding quality for small assembly plates. Under the conditions of single plates with different groove positions and gaps, when the gap was 4 mm, processing efficiency increased by 7.35%, and processing time was reduced by 10.2%; when the gap was 5 mm, processing efficiency increased by 10.7%, and processing time decreased by 7.39%. The welding formation rate for the overall processing of single plate panels and web grooves increased by 11.48%, total material consumption decreased by 13.4%, and unit material consumption decreased by 13.5%. For mass production of small assembly plates of the same specifications, processing time was reduced by 16.7%, and there was a 41.4% reduction in costs. The equipment effectively addresses the low level of automation and heavy dependence on traditional manual processing in the shipbuilding industry, contributing to cost reduction and efficiency improvement.

Keywords: rail-mounted automatic welding equipment; small assembly plates; robotic arm; mechanical design; simulation analysis

Citation: Cai, Y.; Yu, G.; Yu, J.; Ji, Y. Orbital-Based Automatic Multi-Layer Multi-Pass Welding Equipment for Small Assembly Plates. *Appl. Sci.* **2024**, *14*, 10878. https://doi.org/10.3390/app142310878

Academic Editor: Francesco Tornabene

Received: 18 October 2024
Revised: 21 November 2024
Accepted: 21 November 2024
Published: 24 November 2024

1. Introduction

With the development of intelligent technology, the manufacturing industry has entered a stage of deep integration of informatization, automation, and intelligence, and international research and application of automation equipment have become more widespread [1–6]. To address the issue of insufficient demographic dividends, the manufacturing industry urgently needs to develop corresponding automation equipment to achieve the ultimate goal of enhancing production performance and reducing labor costs in the technical field. So far, due to the advent of diversified transformation in the manufacturing industry and the proposal of Industry 4.0, the processes of intelligent manufacturing, industrial internet, and equipment customization have accelerated. Automatic welding equipment with different functions and application scenarios designed through various methods is being initially applied [7–11]. For example, applications include the design and development of automatic welding equipment for pipe welding [12], intelligent handheld

welding devices [13], the design of fixtures for automatic welding equipment [14], and robots developed and applied for automatic welding of box girders and construction steel structures [15].

Small assembly plates serve as fundamental component units in the shipbuilding process. Their simple structure and high demand make them highly suitable for mass production using rail-mounted welding robotic arms equipped with automated welding technology. Traditionally, the processing of small assembly plates relies on manual welding, which results in high labor costs, significant challenges in quality control, prolonged welding cycles, and low production efficiency. This reflects the current state of plate processing in shipyards both domestically and internationally. As labor shortages and the aforementioned technical challenges accelerate the manufacturing industry's transition to "machine substitution," the era of automated welding has arrived. The traditional production model of one person per workstation will gradually shift to an automated production model of one person overseeing an entire production line.

Compared to traditional methods, equipment equipped with welding robotic arms offers faster welding speeds and higher weld seam quality. The use of automated programming technology also allows operators to stay away from harsh production environments. Therefore, in the context of manufacturing process transformation, designing a rail-mounted automatic welding device capable of multi-layer and multi-pass welding serves as a pioneer for intelligent, large-scale, and continuous production of structural components, possessing significant application value.

This equipment integrates mechanical design technology, simulation analysis technology, welding technology, robotics, and automatic processing technology, enabling efficient and precise welding operations. It is a key piece of equipment in intelligent manufacturing both domestically and internationally [16]. By moving along a predetermined track and carrying the necessary functional modules to weld workpieces, the device achieves stable welding quality and production efficiency. However, there are currently few comprehensive studies or available design and analysis schemes for rail-mounted automatic welding equipment utilizing welding robotic arms. Completing the design and analysis of this equipment can provide a theoretical foundation and important data support for subsequent research and production work. The mechanical structure of the rail-mounted automatic welding equipment designed and developed in this paper includes specialized fixing mechanisms, installation and bearing mechanisms, quick-plug mechanisms, and moving mechanisms. The finite element analysis of these mechanisms and equipment testing presented in the following sections provide a basis for further practical applications.

The remainder of this paper is organized as follows. Section 2 introduces the mechanical structure design and analysis of the rail-mounted automatic welding equipment, including its working system and operational logic. Section 3 describes the debugging methods for the welding robotic arm and the simulation analysis methods. Section 4 presents the testing of the automatic welding equipment, the formulation of processing strategies, and the analysis of working conditions. Section 5 conducts comparative experiments between manual and automated multi-layer and multi-pass welding. Finally, in Sections 6 and 7, we provide conclusions and prospects for the future development of this equipment.

2. Design and Analysis of Rail-Mounted Automatic Welding Equipment

2.1. Mechanical Design of the Equipment's Core Mechanisms

As shown in Figure 1, the rail-mounted automatic welding equipment is installed above the working area of small assembly plates. The overall structure includes a rail and base moving mechanism, a fixing mechanism, a quick-plug mechanism, and welding fixtures. The rail is connected to the small assembly work area through the fixing mechanism, and the base can move along the rail. Simultaneously, the base is equipped with a robotic arm and a wire feeder. This part of the design includes the quick-plug mechanism at the end of the robotic arm and a protective mechanism for the visual sensors. The quick-plug

mechanism serves as a connection between the welding torch and the robotic arm, while the protective mechanism provides automatic opening and closing to protect the fragile sensors, enabling the robotic arm to drive the welding torch for automatic welding. Due to the robotic arm's compact structure, small size, and flexible movements, the equipment can perform various types of automated welding in the confined spaces of small assemblies.

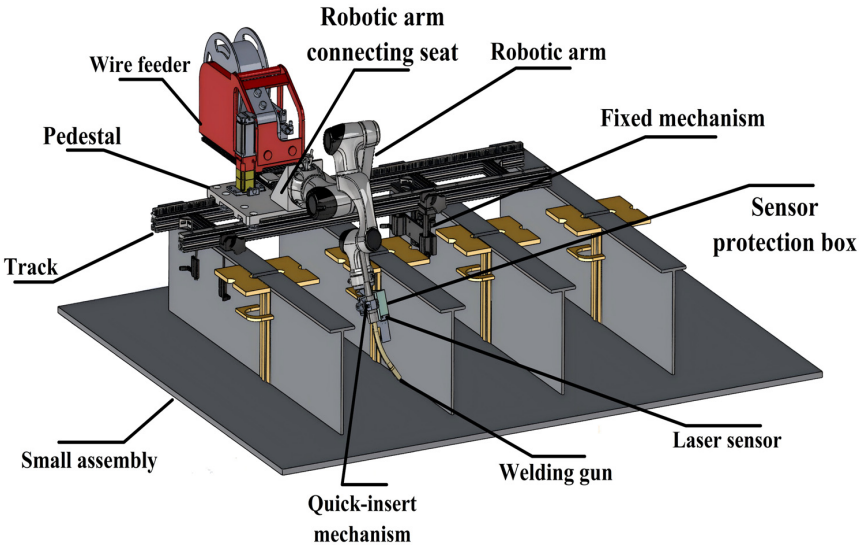

Figure 1. Overview of track equipment.

2.1.1. Mechanical Design of the Rail and Base

As shown in Figure 2, the track consists of two parallel assembled guide rails. These guide rails are constructed from multiple profiled supports and single-flanged guide rails, mechanically installed across the small assembly workpiece. The profiled supports and vertical supports within the guide rails form a ladder-shaped structure, enhancing the track's stability and strength to prevent deviation or deformation. The motor shaft drives the end gear to mesh with the rack and, in coordination with the rollers, moves the base mechanism along the single-flanged guide rail. The rollers have a circumferential groove along the axial direction that matches the edge of the single-flanged guide rail. The two engage with each other, providing precise guidance for the base and reducing frictional losses.

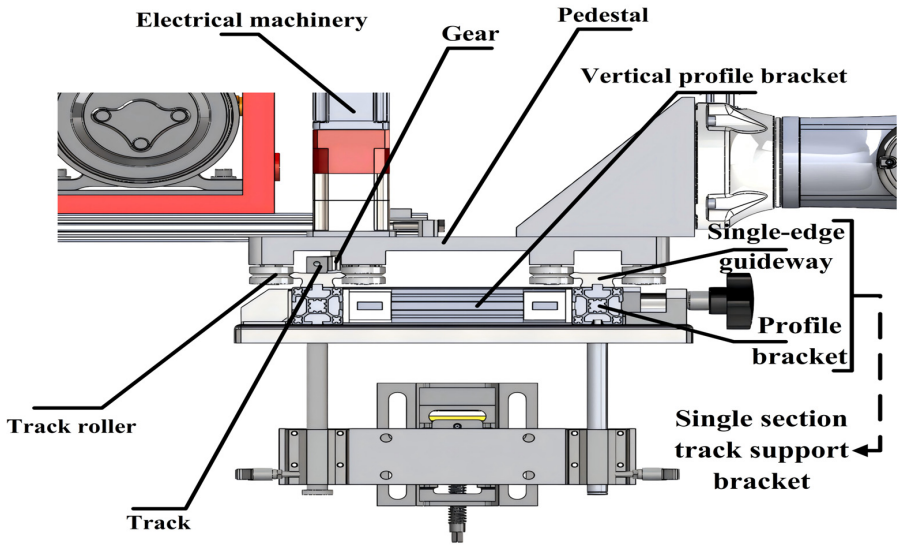

Figure 2. Partial diagram of the track and base.

2.1.2. Mechanical Design of the Fixing Mechanism

As shown in Figure 3, the fixing mechanism mainly comprises a rail clamp and a small assembly clamp. The rail clamp adopts a vise structure, clamping both sides of the rail from below. Support plates and clamps are fixed at both ends of the upper surface of the base plate, and a clamping block is placed between the fixed seat and the support plate. The guide slot of the fixed seat engages with the clamping block, serving a guiding function. An adjusting screw rod provides clamping force to the rail. The small assembly clamp utilizes a flat-jaw clamp structure to clamp the small assembly panel from the side. Consequently, the two clamps work together to quickly install and secure the rail in the working environment. Parallel guide rods and adjusting sliders are arranged beneath the base plate. The plane facing the small assembly is equipped with slider connecting plates and threaded holes, where the small assembly clamp is fixedly connected on top via screws. An adjustable positioning handle is provided on the side of the adjusting slider. By adjusting the slider and the base plate, the height of the rail can be adjusted.

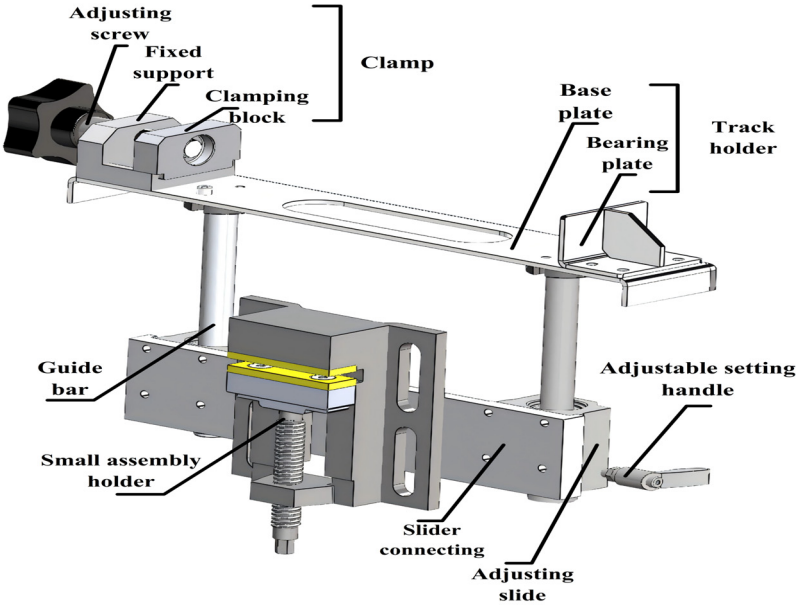

Figure 3. Schematic of fixing mechanism.

2.1.3. Mechanical Design of the Quick-Plug Mechanism and Welding Fixtures

The quick-plug mechanism includes connector components, as shown in Figure 4. This mechanism enables rapid coupling between the welding torch and the robotic arm, facilitating disassembly, transportation, maintenance, and replacement. A connecting base that can be flange-mounted is installed at the end of the robotic arm. A vertical plate is set at the terminal of the robotic arm to mount a welding torch clamp for holding the welding torch. A visual sensor is installed inside a protective box on the connecting base. Locking screws press and secure the welding torch clamp and the connecting base together. The mating surfaces of the connecting base and the welding torch clamp are equipped with axially parallel and corresponding conical male and female positioning pins. Bosses and corresponding matching grooves are arranged on the surface of the vertical plate; the locking screw holes and through-holes penetrate the bosses and grooves, respectively. These features work together to enhance the reliability of the connection. Three conical male positioning pins are arranged on the vertical plate, corresponding and matching with threaded sleeves and female positioning pins within threaded holes. This ensures the installation precision of the vertical plate and the welding torch clamp, improving the control accuracy of the robotic arm over the welding torch. An opening and closing cover is installed at the end of the protective box, controlled by a spring hinge and a micro

telescopic cylinder. Its movement direction is aligned along the torque arm of the cover, providing protection for the visual sensor.

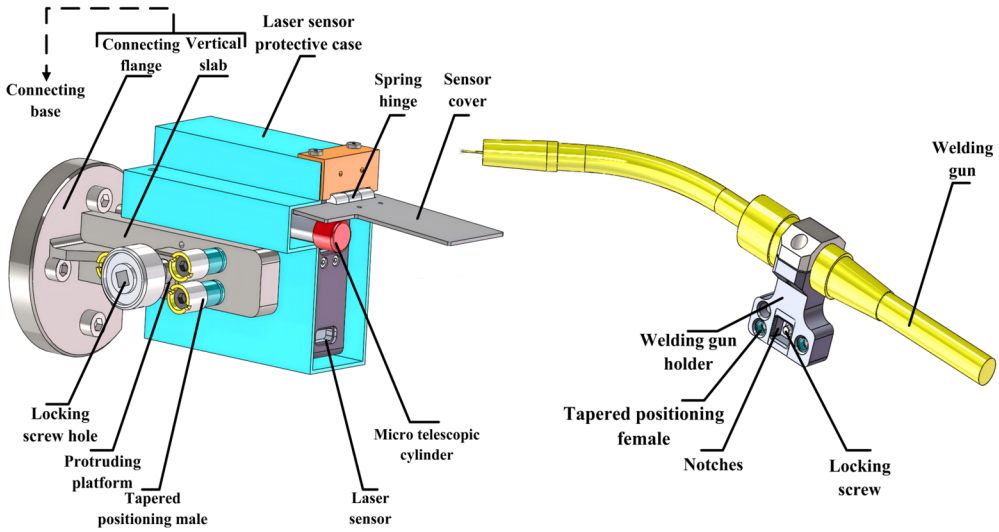

Figure 4. Schematic diagram of quick-insert mechanism.

By organizing the composition and material selection of the mechanical structure [17], the overall mechanical components involved in this equipment and the materials selected in the design are shown in Table 1. The materials listed in the table are the actual materials chosen for the mechanical structures.

Table 1. Equipment composition and material selection details.

Mechanism	Parts	Material
Track mechanism	Rack, Vertical profile bracket, Single-edge guideway Single section track support bracket, Track roller Gear	Aluminum alloy (6061-T6, 6063-T5) Bearing steels (Gcr15) Stainless steels
Base mechanism	Pedestal, Robotic arm connector	Aluminum alloy (7075-T6)
Quick-insert mechanism	Connecting base, Tapered positioning head (male, female), Notches Locking screw hole, Protruding platform, Welding gun holder, Locking screw Laser sensor protective case, Sensor cover Spring hinge Micro telescopic cylinder, Welding gun	Aluminum alloy (7075-T6, 6061-T6) Stainless steels 45# Steel
Fixing mechanism	Adjusting slide, Slider connecting plate, Clamping block, Small assembly holder Adjusting screw Guide bar Adjustable setting handle Base plate, Bearing plate, Fixed support	Aluminum alloy (7075-T6, 6061-T6) 45# Steel Bearing steels (Gcr15) Rigid plastic Carbon structural steel (Q235-A, Q235-B)

2.2. Static Analysis of the Equipment's Core Mechanisms

To prevent deformation and damage caused by excessive loads on parts or mechanisms during operation, this section conducts a static analysis of the aforementioned mechanical design modules and the simplified mechanisms under eccentric loading [18]. Specifically, the analysis involves defining boundary conditions for the model, designing load analysis, material property analysis, structural performance analysis, and result analysis, while also examining high-stress regions and the deformation of the overall model. The mechanism dimension parameter analysis is presented in Table 2, where the parameters exclude the dimensions of external components. Before performing the static analysis, the interaction relationships between mechanical mechanisms and components are practically integrated and organized, fully considering their contact types. This approach clarifies the types and

methods of simulation analysis and enhances the close connection between theoretical analysis and actual conditions. The specific details are provided in Table 3.

Table 2. Mechanism dimension parameter.

Serial Number	Name of Organisation	Length/mm	Breadth/mm	Height/mm	Weight/kg
1	Railcat	430	310	30	6.668
2	Track section	500	256	72.7	4.1255
3	Robotic arm connecting seat	140	140	150	1.3059
4	Fixing mechanism	407	120	272	5.3895
5	Bias load simplification mechanism	779	430	243	10.3635

Table 3. Detailed analysis of the interactivity of mechanical mechanisms and components.

Serial Number	Interaction Objects	Types of Mutual Contact	Types of Interaction
1	Track roller and pedestal	Surface contact	Support bearing
2	Wire feeder and track	Surface contact	Support bearing
3	Track roller and single section track support bracket	Surface contact	Support bearing
4	Track holder and track	Surface contact	Support bearing
5	Track roller and single-edge guideway	Line contact	Meshing drive
6	Adjustable setting handle and adjusting slide	Point contact	Fixed clamping
7	Clamp and track	Surface contact	Fixed clamping
8	Connecting flange and vertical plate	Surface contact	Fixed clamping
9	Small assembly holder and small assembly	Surface contact	Fixed clamping
10	Pedestal and robot arm connecting seat	Surface contact	Fixed clamping
11	Roboic arm and robot arm connecting seat	Surface contact	Fixed clamping
12	Guide bar and adjusting slide	Surface contact	Coupling locking
13	Locking screw and welding gun holder	Point contact	Coupling locking
14	Tapered positioning male and tapered positioning female	Surface contact	Coupling locking
15	Notches and protruding platform	Surface contact	Coupling locking
16	Laser sensor and laser sensor protective case	Surface contact	Coupling locking

The length, width, and height of the finite element model of the simplified eccentrically loaded mechanism correspond to the Z, X, and Y axes of the Cartesian coordinate system, respectively. For the finite element models of the other analysis mechanisms, the length, width, and height also correspond to the Z, X, and Y axes of the Cartesian coordinate system. The static data analysis is presented in Table 4. Fixed constraints with six degrees of freedom are applied to each mechanism. The mesh is divided using tetrahedral solid elements, with both their size and quality adopting global average values. In the following, the actual performance conditions of the mechanical mechanisms are combined with the simulation analysis module of ANSYS 2023 software to derive the corresponding reliability limit values for the analyzed mechanism types. This provides a reliable reference for engineering applications.

Table 4. Statics analysis data.

Serial Number	Name of Organisation	Mesh Size/mm	Mesh Quality	Number of Nodes	Number of Units	Constrained Position
1	Railcart	5	0.7	286,768	177,938	Bottom roller
2	Track section	6	0.6	512,882	146,523	Bottom of guide
3	Robotic arm Connecting seat	5	0.8	56,847	35,403	Install base underside
4	Fixing mechanism	5	0.6	223,900	124,038	Back mounting hole
5	Bias load simplification mechanism	5	0.4	322,139	144,224	Railcart underside

The finite element model and mesh division of the rail cart are shown in Figure 5.

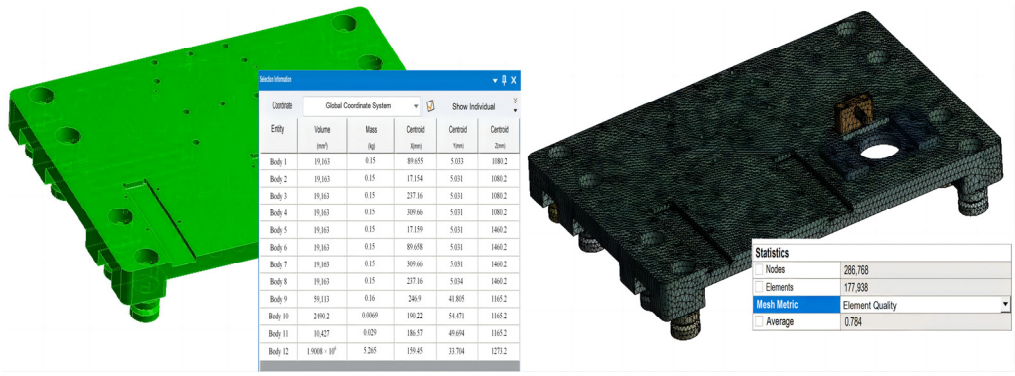

(**a**) (**b**)

Figure 5. Rail cart grid division model diagram. (**a**) Finite element module division diagram. (**b**) Finite element mesh division diagram.

The analysis diagrams of the rail cart are illustrated in Figure 6. A pressure of 0.1876 MPa is applied to the surface of the rail cart, as shown in Figure 6a. The deformation of the rail cart is depicted in Figure 6b, where the maximum deformation of the model is 0.856 mm, occurring on the upper surface of the rail cart. The local and overall equivalent stresses are shown in Figures 6c and 6d, respectively. The maximum equivalent stress is 352.83 Mpa, occurring on the rollers, reaching the yield strength of bearing steel GCr15, which is 353 Mpa. In the simulation analysis for the application conditions or the actual engineering application of the mechanism, if the stress on the rollers approaches their maximum allowable range, the material can be replaced according to the corresponding performance requirements and safety demands, retaining a certain safety margin in the selection of material properties. According to safety regulations, it is necessary to prevent deformation and damage of the mechanism caused by overload on the surface of the rail car to avoid causing simultaneous damage to the equipment mounted on the rail car.

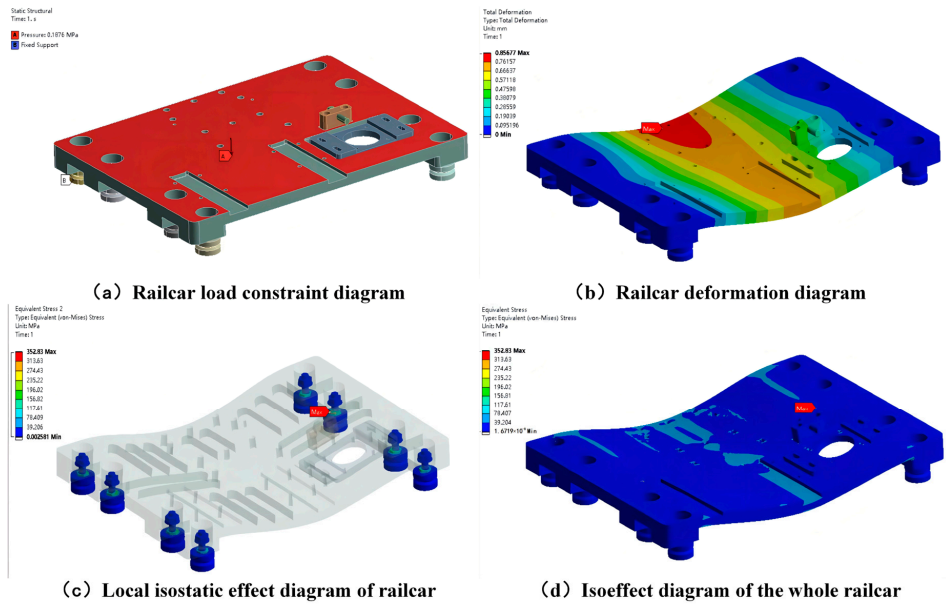

(a) Railcar load constraint diagram (b) Railcar deformation diagram

(c) Local isostatic effect diagram of railcar (d) Isoeffect diagram of the whole railcar

Figure 6. Rail cart analysis diagram.

Since the equipment is mounted on a track, the carrier vehicle must operate while maintaining the stability of the modules installed above the vehicle without interference. The following layout is therefore adopted: The mounting center of the robotic arm instal-

lation base is aligned with the center of the upper surface of the track vehicle. The wire feeder mounting center is offset 66 mm along the *Z*-axis relative to the base, forming an asymmetric layout. This off-center arrangement prevents interference between the wire feeder and the communication and power cables of the robotic arm during the operation of the track-based equipment, ensuring greater flexibility in the movement posture of the welding robot and providing sufficient workspace. A load shift analysis is conducted below. To reduce computational errors from excessive workload, the model is simplified for analysis, with the finite element mesh model shown in Figure 7.

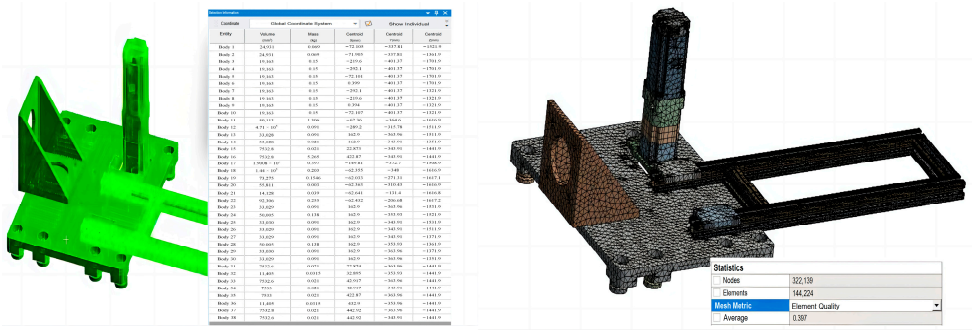

Figure 7. Rail cart grid division model diagram. (**a**) Finite element module division diagram. (**b**) Finite element mesh division diagram.

At one end of the robotic arm mounting base, the load includes its own body, the robotic arm, the welding torch module, and the vision module, totaling 21 kg. At the wire feeder end, the load includes its body and the supporting rail section, totaling 20.3 kg. The loads at both ends are directed vertically downward, and the distance from the robotic arm's center of mass to the center of the rail cart is 682 mm. Therefore, an eccentric concentrated load is applied to the model; as shown in Figure 8a, corresponding normal pressures and gravitational loads are applied to both ends. The deformation results of the robotic arm mounting base are shown in Figure 8b; the maximum deformation is 0.23 mm, occurring at its upper end surface. The overall equivalent stress is depicted in Figure 8c; the maximum equivalent stress is 37.285 MPa, occurring at the junction between the robotic arm mounting base and the rail cart. The maximum equivalent stress at the rail is 26.747 MPa. Both values are much lower than the material's yield strength of 353 MPa, satisfying the structural strength requirements. The overall deformation of the simplified eccentric load mechanism is shown in Figure 8d. Experimental results confirm that this arrangement is reasonable and operates stably.

The finite element mesh model of the rail section is shown in Figure 9. The rail section has a length of 500 mm and is made entirely of aluminum alloy.

As illustrated in Figure 10a, a downward vertical pressure of 9.756 MPa is applied to the aluminum alloy rack of the rail section. The deformation diagram of the rail section is shown in Figure 10b, where the model's maximum deformation is 0.09 mm. The local and overall equivalent stresses are presented in Figures 10c and 10d, respectively. The maximum equivalent stress is 269.96 MPa, located at the guide rail position of the rail section, reaching the yield strength of 270 MPa for 6063-T5 aluminum alloy. At this point, the maximum equivalent stress for aluminum alloy 6061-T6 is 50.086 MPa, which does not reach its yield strength of 275 MPa. In the simulation analysis for the application conditions or the actual engineering application of the mechanism, if the stress on the rails approaches their maximum allowable range, the material can be replaced according to the corresponding performance requirements and safety demands, retaining a certain safety margin in the selection of material properties. According to safety regulations, it is necessary to prevent deformation or even fracture of the rails caused by overload on their surface to avoid derailing or the equipment running off the track due to rail deformation or uneven stress, which could affect equipment operation and processing.

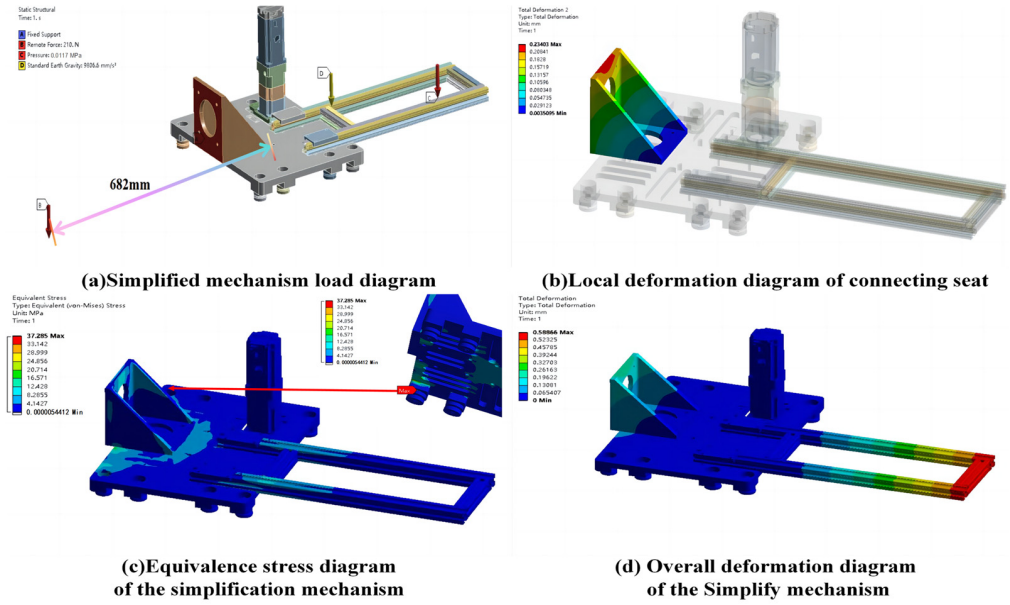

Figure 8. Simplified mechanism bias load analysis diagram.

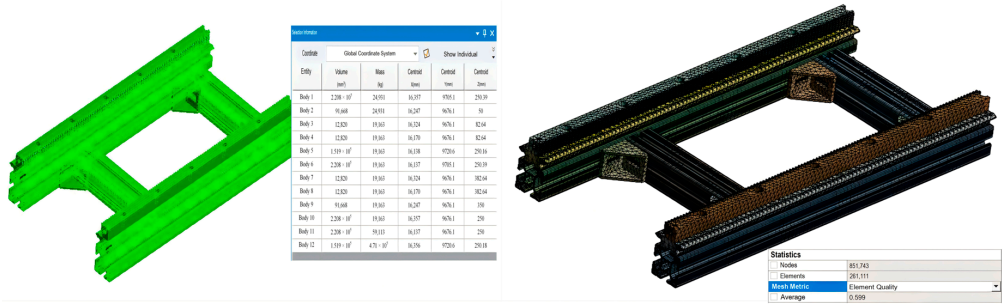

Figure 9. Track section grid division model diagram. (**a**) Finite element module division diagram. (**b**) Finite element mesh division diagram.

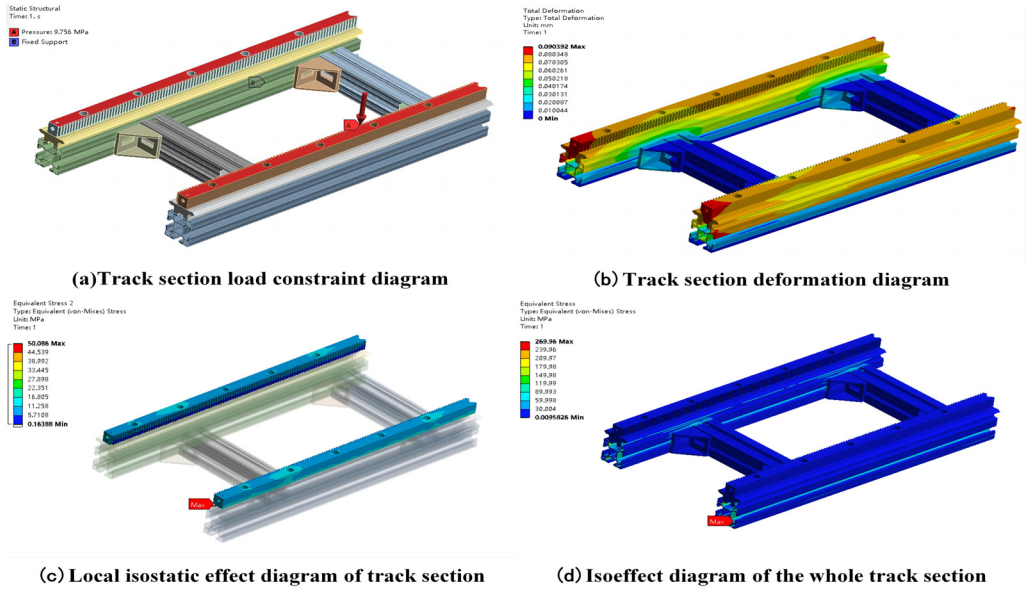

Figure 10. Track section analysis diagram.

The robotic arm mounting base is made entirely of aluminum alloy, and its finite element mesh model is shown in Figure 11.

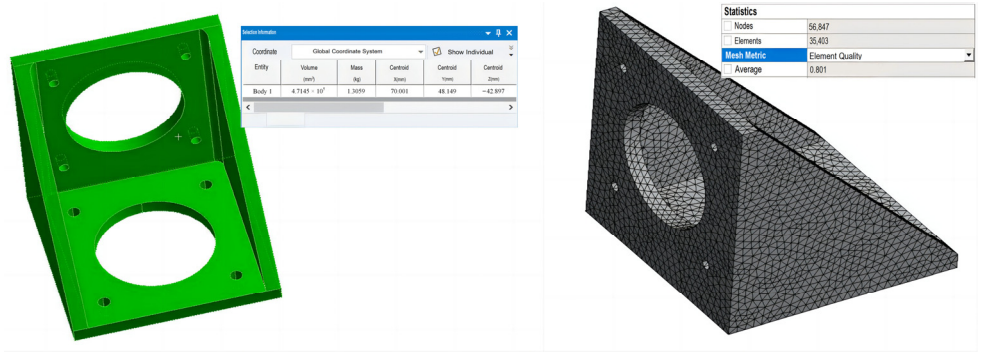

(**a**) (**b**)

Figure 11. Robotic arm connecting seat grid division model diagram. (**a**) Finite element module division diagram. (**b**) Finite element mesh division diagram.

As illustrated in Figure 12a, a pressure of 2.62 MPa is applied to the back surface of the robotic arm mounting base, directed perpendicularly outward. The deformation diagram of the robotic arm mounting base is obtained, as shown in Figure 12b, where the model's maximum deformation is 1.509 mm. The local and overall equivalent stress diagrams are presented in Figures 12c and 12d, respectively; the maximum equivalent stress is 506.8 MPa, reaching the yield strength of 505 MPa for 7075-T6 aluminum alloy.

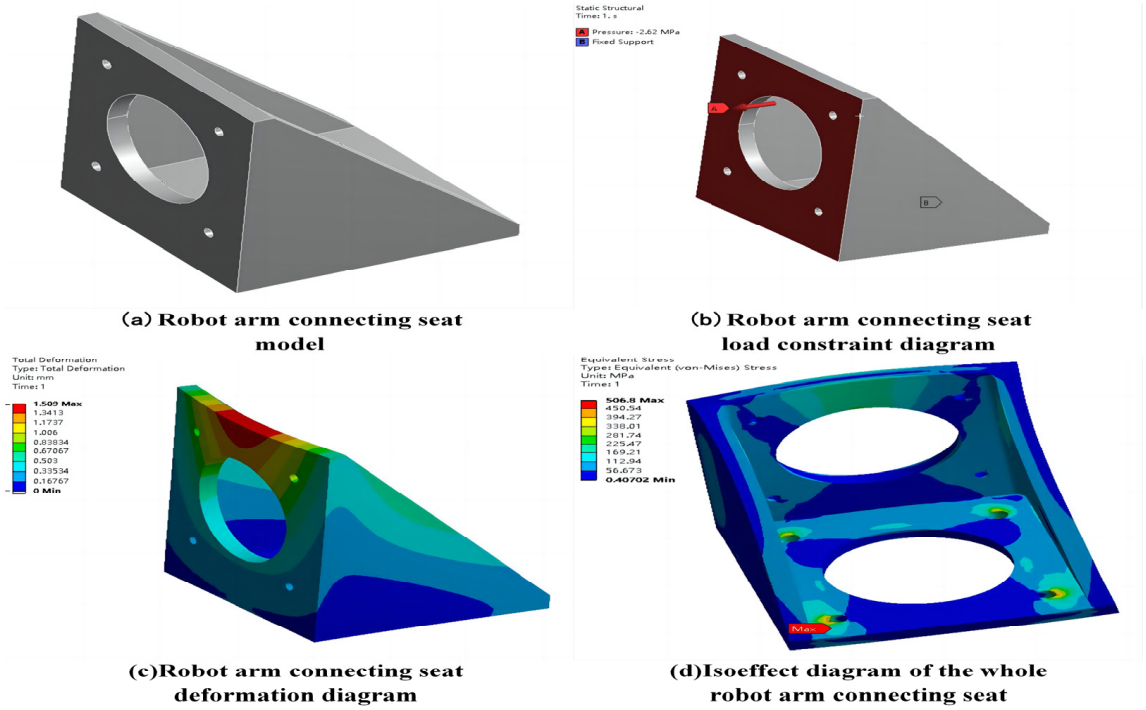

Figure 12. Robotic arm connecting seat analysis diagram.

The finite element mesh model of the fixing mechanism is shown in Figure 13.

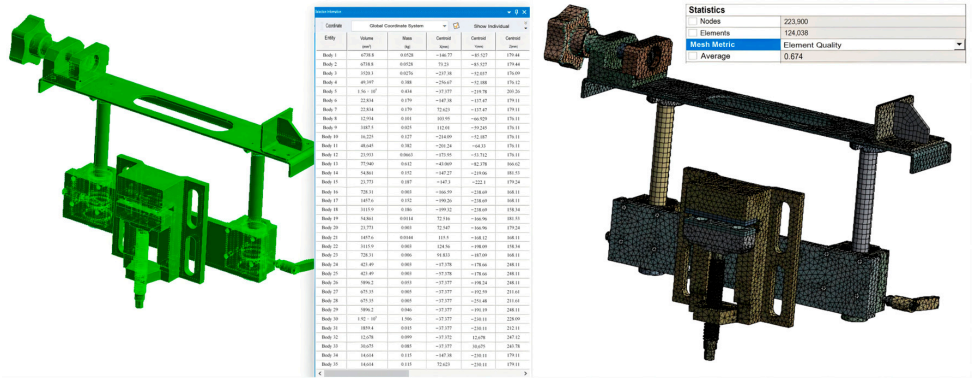

Figure 13. Fixing mechanism grid division model diagram. (**a**) Finite element module division diagram. (**b**) Finite element mesh division diagram.

As shown in Figure 14a, a concentrated force of 39,053 N is applied to the surface of the round rod of the fixing mechanism, directed vertically upward along the axial direction of the rod. The deformation of the model and the ultimate friction load diagram within the fixing mechanism are shown in Figure 14b, where the maximum deformation of the connecting rod is 0.0093 mm. The overall equivalent stress diagram of the connecting rod is presented in Figure 14c; the maximum equivalent stress is 505 MPa, occurring inside the adjusting slider, reaching the yield strength of 505 MPa for its material, 7075-T6 aluminum alloy. With the constraint conditions unchanged, an 8.81 MPa pressure is applied to the upper and lower surfaces of the clamping block of the fixing mechanism in opposite directions, as shown in the designed ultimate clamping force diagram in Figure 14d. The deformation diagram and equivalent stress diagram of the vise base are shown in Figures 14e and 14f, respectively. The maximum deformation of the vise base is 0.021 mm, and the maximum equivalent stress is 205.98 MPa, occurring at the contact area between the clamping block and the threads, reaching the yield strength of 205 MPa for its material, 6061-T6 aluminum alloy.

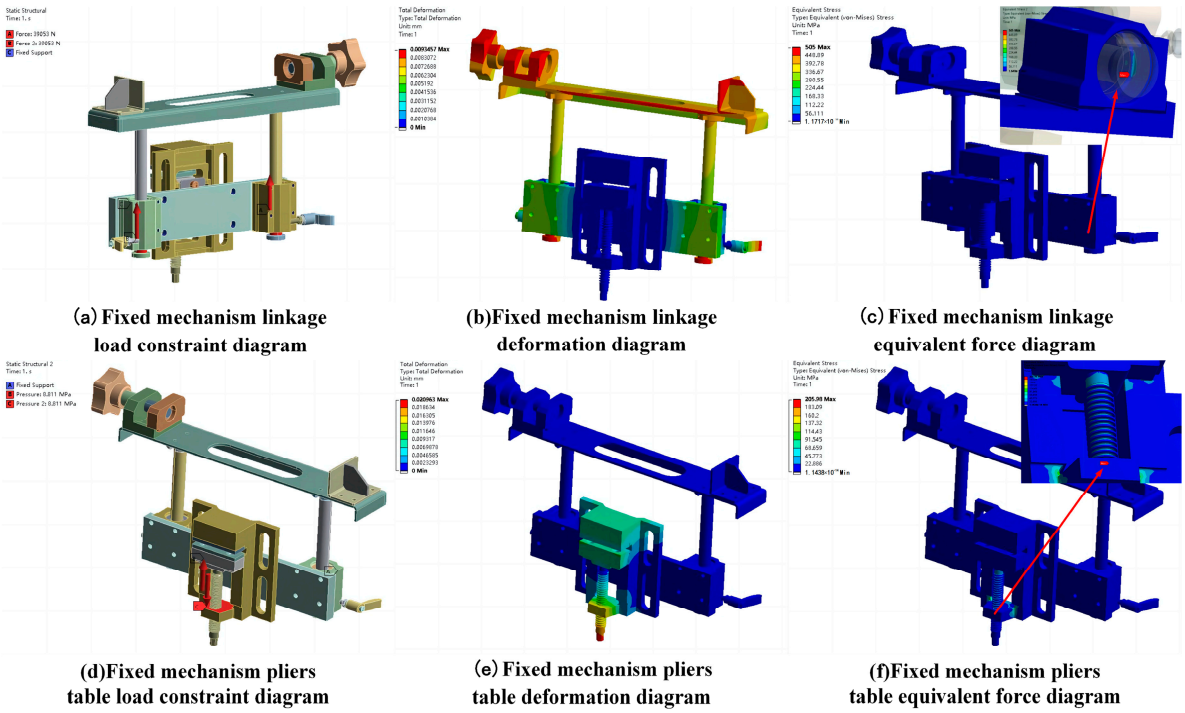

Figure 14. Fixing mechanism analysis diagram.

2.3. Operational Logic and Workflow of the Equipment

2.3.1. Operational Logic

The operational logic and workflow of the rail-mounted automatic welding equipment include overall mechanical installation, power distribution and supply, load bearing, and communication connections. The logical components of this operating system can be understood in conjunction with Figure 15.

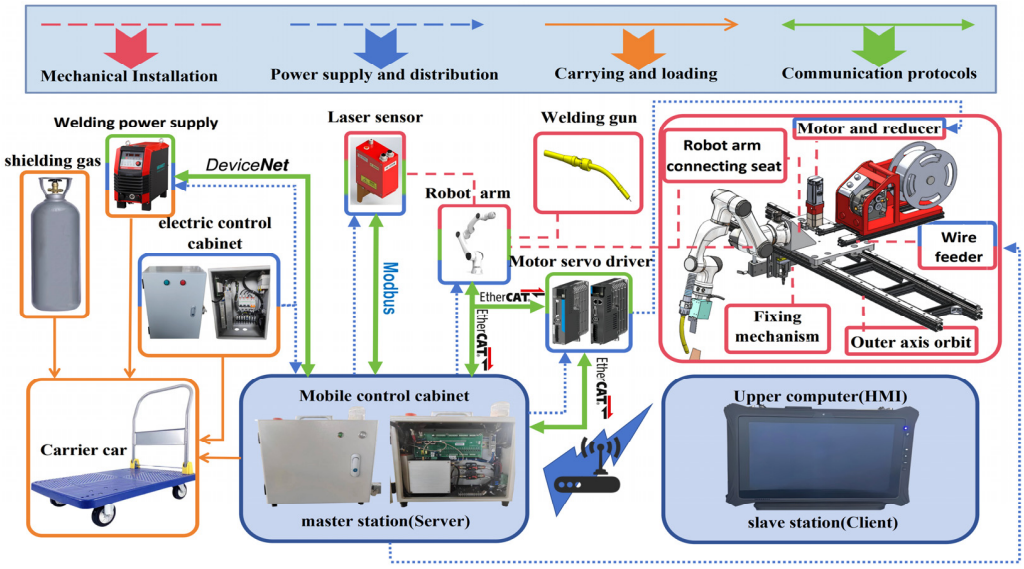

Figure 15. Overall working logic diagram of equipment.

The electric control cabinet supplies power to the welding machine and the main station, which is a mobile control cabinet. The main station provides power to the motors and servo drives, reducers, wire feeders, laser sensors, and the robotic arm body. The software control adopts a client/server (C/S) architecture with modular implementation. The slave station (client), namely the upper computer (HMI), connects wirelessly to the main station to improve transmission efficiency and reduce unnecessary safety hazards caused by cables. The upper computer achieves control over the welding machine, robotic arm, laser sensor, and motor servo drives by invoking services and also handles overall timing, algorithms, and strategies. The welding machine, laser sensor, and robotic arm communicate with the main station using DeviceNet, ModbusTCP, and EtherCAT protocols, respectively. The output and input ports of the motor servo drives are connected to the motors and the main station, respectively; together with the main station and robotic arm, they use the EtherCAT protocol, adding an external axis control system. The laser sensor and welding torch are mounted on the robotic arm, which, along with the motor, reducer, and wire feeder, is installed on the base of the rail cart. The carrier vehicle bears the shielding gas, welding machine, electric control cabinet, and main station, with the type of shielding gas selectable according to requirements.

2.3.2. Workflow

After the robotic arm is positioned at the origin, the upper computer controls the robotic arm to perform scanning and welding. During scanning, the robotic arm adopts a divide-and-conquer strategy: first obtaining the approximate outline of the entire fixture or target, then performing detailed scanning based on the type of plate to be processed. The upper computer conducts corresponding visual analysis of the entire fixture based on the scanning results; the visual analysis system employs algorithms such as extremum strategies, filtering, and cyclic verification. After processing, the upper computer statistically summarizes and generates the welding paths and, in coordination with the correspond-

ing welding processes, completes the actual welding of each path segment. The overall operational equipment diagram is shown in Figure 16.

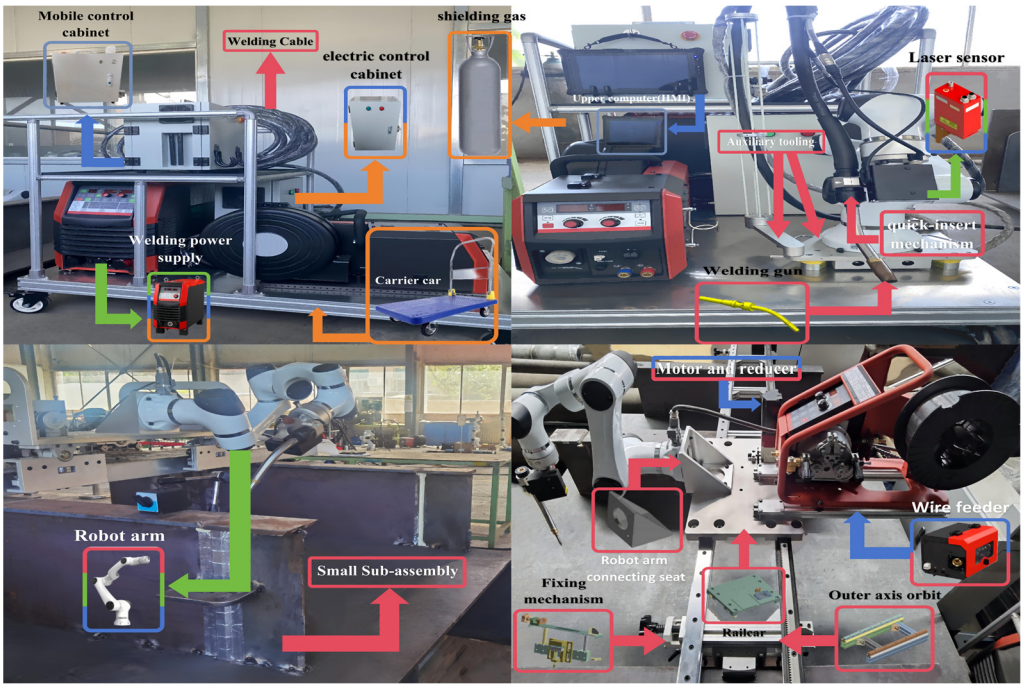

Figure 16. Overall operating equipment summary diagram.

The detailed workflow of the equipment is as follows: Before operation, the robotic arm along with the external axis system can be set to manual, teach, or automatic modes. It can also perform demonstrations using welding simulation or trajectory simulation. During operation, the electric control cabinet remains powered on and is connected to the mobile control cabinet. The mobile control cabinet is equipped with a main control board, IO board, adapter board, laser module, switching power supply, network switch, power cables, and data cables. The main control board, adapter board, and IO board are responsible for receiving externally input discrete signals, analog signals, and digital signals. The network switch connects the upper computer (HMI) to the adapter board; signals are transmitted to the main control board via communication protocols, completing the overall information transmission process. The equipment's welding cables, communication cables, and sensors adopt protective designs using auxiliary fixtures and protective covers. After welding, the database can be updated and iterated according to different working condition types, and new scanning strategies and welding processes can be formulated. In terms of technical features, the working modes of the rail-mounted automatic welding equipment can be divided into three types: upright installation, inverted installation, and side installation. Due to the stability requirements of welding conditions and the need for specific welding postures, this design adopts the upright installation arrangement. The specific type analysis is shown in Table 5.

Table 5. Job type detail.

Working Method	Applicable Scene	Vantage	Limitations
Installed above the track	Specified range welding	Stabilization	Localised movement restricted
Installed under the track	Automatic handling	Wide operating range	Load capacity limited
Installed on the side of the track	Automated assembly	High working accuracy	Complex installation and maintenance

3. Equipment Debugging and Simulation Analysis

3.1. Debugging of the Robotic Arm

Before commissioning, it must first be specified that the movement direction of the external axis of the rail is the Z direction in the world coordinate system. The robotic arm, wire feeder, tool flange, quick-plug mechanism, welding torch, and laser sensor are installed onto the bearing mechanism. After the mechanical installation is completed, TCP calibration and laser calibration of the robotic arm are performed. This study adopts the hand-eye calibration method and recommends maintaining a unified calibration posture reference before calibration to prevent precision issues and mechanical arm failures such as lock-up. The starting point of calibration is the flange, which is the end part of the robotic arm. The coordinate system relationships comply with the Cartesian right-hand coordinate system rule shown in Figure 17. During calibration, the coordinate system coincides with the earth coordinate system at the base of the robotic arm, placed at the central position of the robotic arm base, and has the same orientation as the robotic arm's world coordinate system.

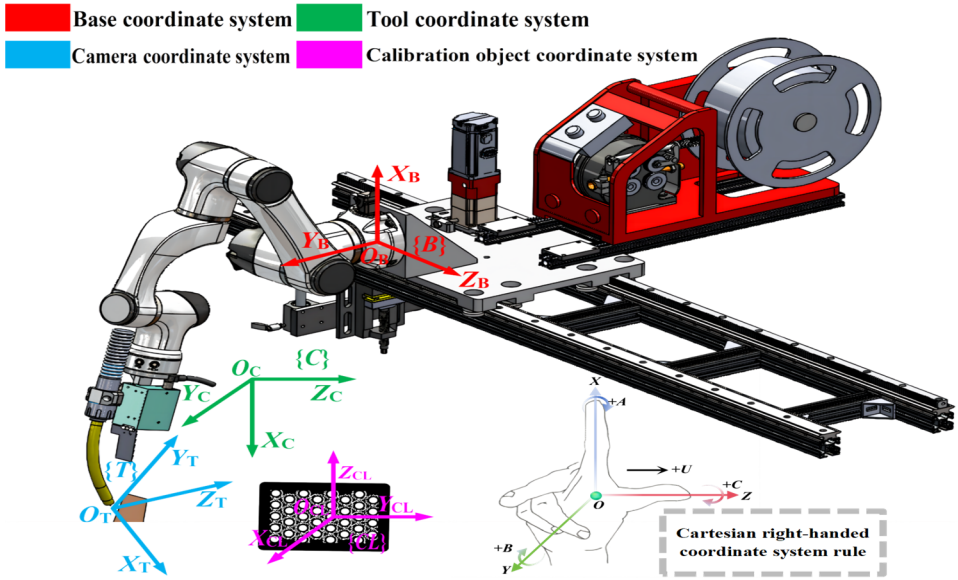

Figure 17. Relative diagram of the coordinate system for the calibration process.

The upper computer processes the hand-eye coordinate system relationship through calibration algorithms and the internal and external parameter matrices of the laser sensor. It converts the relative relationship between the origin of the robotic arm's Cartesian coordinate system relative to the robotic arm flange into the relative spatial relationship between the origin of the robotic arm base's Cartesian coordinate system and the sensor's laser scanning point, as shown in Figure 17. The calibration process requires completing the transformations among the four coordinate systems B, T, C, and CL to obtain the coordinate conversion relationships between two-dimensional pixel coordinates and the spatial coordinate system. The visual recognition results are transferred to the robotic arm's coordinate system, thereby achieving precise robotic arm motion control and visual guidance. In Figure 17, {B} represents the robotic arm base coordinate system, {T} represents the laser sensor coordinate system, {C} represents the laser sensor coordinate system, and {Cl} represents the calibration object coordinate system.

For the coordinates of the same point p in any two Cartesian coordinate systems $\{M_1\}$ and $\{M_2\}$ in three-dimensional space, the transformation matrix (1) is a 4×4 matrix, which can be represented as the combination H of rotation R and translation T.

$$H = \begin{bmatrix} R & T \\ 0 & 1 \end{bmatrix} = \begin{bmatrix} r_{11} & r_{12} & r_{13} & t_x \\ r_{21} & r_{22} & r_{23} & t_y \\ r_{31} & r_{32} & r_{33} & t_z \\ 0 & 0 & 0 & 1 \end{bmatrix} \tag{1}$$

In the Equation (1), the submatrix composed of R represents the rotation matrix, and $T(t_x, t_y, t_z)$ represents the translation vector. The coordinates of point p in $\{M_1\}$, (x_1, y_1, z_1) are transformed into homogeneous coordinates $(x_2, y_2, z_2, 1)$, thereby obtaining the coordinates of point p in $\{M_2\}$, (x_2, y_2, z_2).

$$\begin{bmatrix} x_2 \\ y_2 \\ z_2 \\ 1 \end{bmatrix} = \begin{bmatrix} r_{11} & r_{12} & r_{13} & t_x \\ r_{21} & r_{22} & r_{23} & t_y \\ r_{31} & r_{32} & r_{33} & t_z \\ 0 & 0 & 0 & 1 \end{bmatrix} \begin{bmatrix} x_1 \\ y_1 \\ z_1 \\ 1 \end{bmatrix} \tag{2}$$

The following coordinate system transformation relationships are expressed as Euclidean transformation matrices: BHCl represents the transformation from the base coordinate system {B} to the calibration object coordinate system {Cl}. CHT represents the transformation from the laser sensor coordinate system {C} to the TCP coordinate system {T}. This is the "eye-in-hand" relationship; regardless of how many movements occur, the positional relationship between the robotic arm base and the calibration board remains unchanged, and the positional relationship between the laser sensor and the TCP remains unchanged—that is, BHCl and CHT are constants. CHCl represents the transformation from the laser sensor coordinate system {C} to the calibration object coordinate system {Cl}, obtained through laser sensor calibration. BHT represents the transformation from the base coordinate system {B} to the TCP coordinate system {T}, derived from the robotic arm calibration system. When the robotic arm moves from position 1 to position 2, the following transformation relationships hold:

$$\{B\} = BHT_1 \cdot \{T\}_1 \tag{3}$$

$$\{T\}_1 = CHT^{-1} \cdot \{C\}_1 \tag{4}$$

$$\{C\}_1 = CHCl_1 \cdot \{Cl\} \tag{5}$$

Based on Equations (3)–(5), we obtain (6):

$$\{B\} = BHT_1 \cdot CHT^{-1} \cdot CHCl_1 \cdot \{Cl\} \tag{6}$$

Similarly, after the robotic arm moves to position 2, we obtain (7):

$$\{B\} = BHT_2 \cdot CHT^{-1} \cdot CHCl_2 \cdot \{Cl\} \tag{7}$$

Combining and rearranging Equations (6) and (7), we derive (8):

$$BHT_2^{-1} \cdot BHT_1 \cdot CHT^{-1} = CHT^{-1} \cdot CHCl_2 \cdot CHCl_1^{-1} \tag{8}$$

If we let $X = CHT^{-1}$, $A = BHT_2^{-1} \cdot BHT_1$, $B = CHCl_2 \cdot CHCl_1^{-1}$, we deduce (9):

$$A \cdot X = X \cdot B \tag{9}$$

To solve the problem in the form of Equation (9), we first need to complete the transformation from the base coordinate system to the TCP coordinate system. The rotation matrix is calculated based on the angles of the robotic arm. This paper adopts a specific

ZYX Euler angle rotation matrix form to solve BHT. The rotation matrices of the three angles are as shown in Equation (10), where a, b, and c correspond to the (yaw), (pitch), and (roll) angles in the ZYX Euler angles.

$$\begin{cases} \boldsymbol{R}_x(a) = \begin{bmatrix} 1 & 0 & 0 \\ 0 & \cos a & -\sin a \\ 0 & \sin a & \cos a \end{bmatrix} \\ \boldsymbol{R}_y(b) = \begin{bmatrix} \cos b & 0 & \sin b \\ 0 & 1 & 0 \\ -\sin b & 0 & \cos b \end{bmatrix} \\ \boldsymbol{R}_z(c) = \begin{bmatrix} \cos c & -\sin c & 0 \\ \sin c & \cos c & 0 \\ 0 & 0 & 1 \end{bmatrix} \end{cases} \tag{10}$$

Following the sequence of ZYX Euler angles to complete the rotations, multiplying the three matrices yields (11), which expands into (12):

$$R = R_x(a)R_y(b)R_z(c) \tag{11}$$

$$R = \begin{bmatrix} \cos b \cos c & -\cos a \sin c + \sin a \sin b \cos c & \sin a \sin c + \cos a \sin b \cos c \\ \cos b \sin c & \cos a \cos c + \sin a \sin b \sin c & -\sin a \cos b + \cos a \sin b \sin c \\ -\sin b & \sin a \cos b & \cos a \cos b \end{bmatrix} \tag{12}$$

A schematic diagram of the ZYX Euler angle rotation is shown in Figure 18.

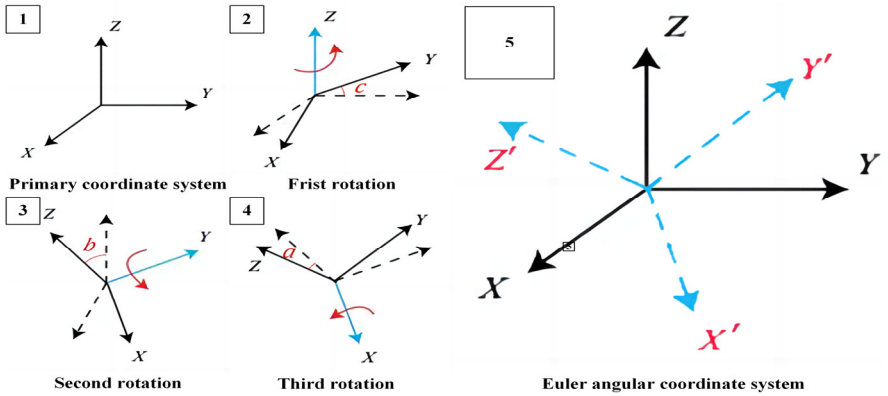

Figure 18. Schematic of Euler angle rotation.

The homogeneous matrix $BHT_{(T)}$ is calculated based on R:

$$\boldsymbol{T} = \left(\begin{bmatrix} & \boldsymbol{R} & & \boldsymbol{t_{0x}} \\ & & & \boldsymbol{t_{0y}} \\ & & & \boldsymbol{t_{0z}} \\ \boldsymbol{0} & \boldsymbol{0} & \boldsymbol{0} & \boldsymbol{1} \end{bmatrix} \right)^{-1} \begin{bmatrix} \boldsymbol{t_{tx}} \\ \boldsymbol{t_{ty}} \\ \boldsymbol{t_{tz}} \\ \boldsymbol{1} \end{bmatrix} = \begin{bmatrix} \boldsymbol{T_x} \\ \boldsymbol{T_y} \\ \boldsymbol{T_z} \\ \boldsymbol{1} \end{bmatrix} \tag{13}$$

In Equation (13), (t_{0x}, t_{0y}, t_{0z}) are the origin of the base coordinate system, (t_{tx}, t_{ty}, t_{tz}) are the origin of the TCP, and (T_x, T_y, T_z) record the values of $\boldsymbol{T}$, denoted as $\boldsymbol{BHT} - \boldsymbol{T}$, which will be used for the calculation of the orthogonal vectors of $\{\boldsymbol{C}\}$. In the actual calibration, the eight-point calibration method shown in Figure 19 is adopted for the TCP. These eight points are non-colinear and uniformly distributed within the working space of the robotic arm. The calibration postures need to be manually set, leaving a margin under rotational limit conditions to prevent the robotic arm from locking up or generating singularities. Under the world coordinate system, the robotic arm is operated to sequentially collect and record the position and posture information of the TCP relative to the calibration object. This calibration algorithm uses the J5 axis as the main control axis. In Figure 19a, the TCP

of the robotic arm needs to be perpendicular to the calibration object when taking points. In Figure 19b–h, A and B represent the rotational directions around the X and Y axes in the robotic arm's world coordinate system, and the new posture changes are made as large as possible compared to the previous ones. After point acquisition is completed, calculate the errors. Once they are within the allowable range, operate the robotic arm under the world coordinate system to make its TCP perpendicular to the calibration object and rotate the robotic arm around the A, B, and C axes to check the degree of alignment. Upon passing the verification, the TCP calibration is completed. The smaller the calibration error, the higher the working efficiency and precision of the robotic arm, except when there are errors in the robotic arm itself.

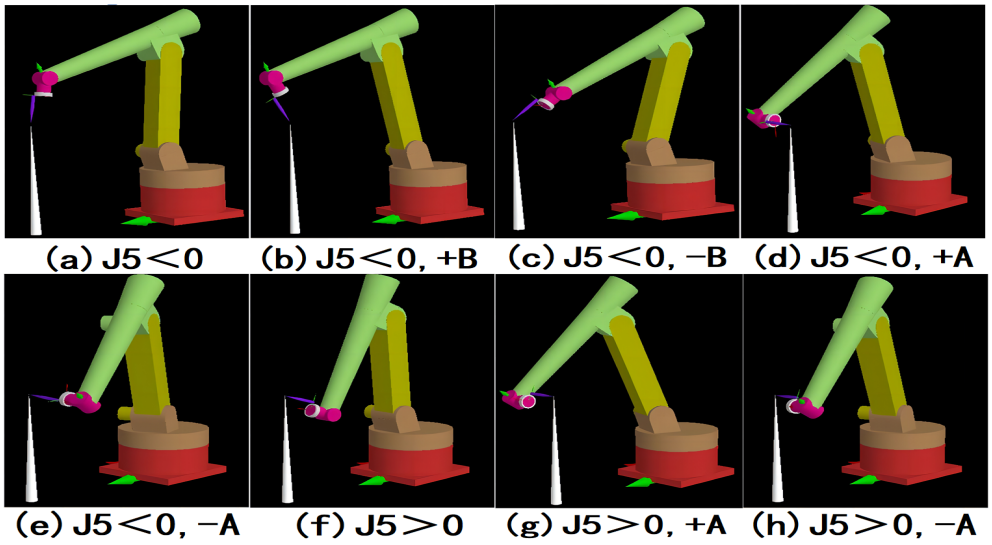

Figure 19. Robotic arm TCP eight-point calibration diagram.

In automatic welding technology, visual sensors are an important component driving the development of intelligent welding [19]. As the "eyes" of robotic arms, visual sensors are also a necessary means of assisting operations [20,21]. Next, we will complete the solution and calibration of the transformation relationship of the laser sensor to achieve precise perception of position and orientation, ensuring the accuracy and stability of scanning recognition. First, we introduce the laser sensor model and use its intrinsic and extrinsic parameter matrices for solving. Both map points from the 3D world to the 2D image plane, i.e., conversion between dimensions. The intrinsic parameters IP, related to the internal characteristics of the laser sensor, can be represented as follows (14):

$$\boldsymbol{IP} = \begin{bmatrix} f & 0 & x_0 \\ 0 & f & y_0 \\ 0 & 0 & 1 \end{bmatrix} \tag{14}$$

The extrinsic parameters describe the position and orientation of the laser sensor in the world coordinate system, allowing for the transformation from world coordinates to laser sensor coordinates. That is, the extrinsic parameters are $EP = H$. Based on the derivation of the relationship between intrinsic and extrinsic parameters, after performing homogenization operations on the point $p(u_0, v_0)$ from the 2D image plane and its spatial coordinates $p(x_0, y_0, z_0)$, we obtain the model of the laser sensor, represented as (15).

$$\lambda \begin{bmatrix} u_0 \\ 0 \\ v_0 \\ 1 \end{bmatrix} = \boldsymbol{IP} \cdot \boldsymbol{EP} \cdot \begin{bmatrix} x_0 \\ y_0 \\ z_0 \\ 1 \end{bmatrix} \quad \textit{or} \quad \lambda \begin{bmatrix} u_0 \\ 0 \\ v_0 \\ 1 \end{bmatrix} = \begin{bmatrix} f & 0 & x_0 \\ 0 & f & y_0 \\ 0 & 0 & 1 \end{bmatrix} \cdot \begin{bmatrix} r_{11} & r_{12} & r_{13} & t_x \\ r_{21} & r_{22} & r_{23} & t_y \\ r_{31} & r_{32} & r_{33} & t_z \\ 0 & 0 & 0 & 1 \end{bmatrix} \cdot \begin{bmatrix} x_0 \\ y_0 \\ z_0 \\ 1 \end{bmatrix} \tag{15}$$

In (15), λ refers to degrees of freedom. During the process of moving from 3D space (laser sensor coordinates) to 2D space (captured image coordinates), one degree of freedom is reduced, particularly depth. The intrinsic parameters focal length (λ) and principal point $c_0(x_0, y_0)$ are provided by the laser sensor. Subsequently, combining the above matrices to solve for the extrinsic parameters, this paper obtains CHT by utilizing the projection information of five different calibration points. The calibration transformation relationship is shown in Figure 20.

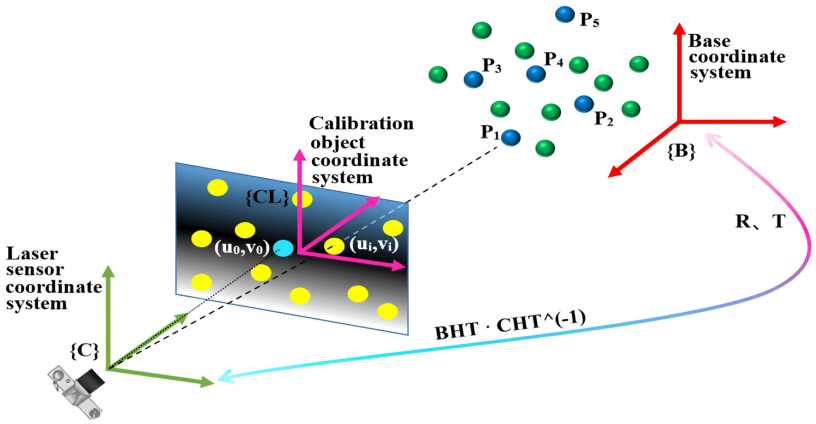

Figure 20. Calibration conversion relationship diagram.

Using the laser five-point calibration method, a calibration starting center point u_c, v_c and four calibration points at different positions with coordinates u_i, v_i on the target plane are selected, along with the pose parameters of the base coordinate system, with coordinates (x_i, y_i, z_i) and angles (a_i, b_i, c_i), where $i = 1, 2, 3, 4, 5$. Then the offset matrix $\boldsymbol{M}$ is prepared.

$$M = \begin{bmatrix} u_1 & v_1 & 1 \\ u_2 & v_2 & 1 \\ u_3 & v_3 & 1 \\ u_4 & v_4 & 1 \\ u_5 & v_5 & 1 \end{bmatrix} \tag{16}$$

Calculation of $\boldsymbol{BHT} - \boldsymbol{T}$ is performed five times according to Equation (13) to obtain $\boldsymbol{T}_i(T_{i,x}, T_{i,y}, T_{i,z})$. Based on $\boldsymbol{M}$ and $\boldsymbol{T}$, the rotation and translation information is extracted from their product. Then, according to the required orthogonality, the three orthogonal vectors are computed (17).

$$\begin{cases} \left(R_1 = M^{+} \begin{bmatrix} T_{1,x} \\ T_{2,x} \\ T_{3,x} \\ T_{4,x} \\ T_{5,x} \end{bmatrix} = \begin{bmatrix} r_{11} \\ r_{13} \\ x_r \end{bmatrix}\right)\left(R_2 = M^{+} \begin{bmatrix} T_{1,y} \\ T_{2,y} \\ T_{3,y} \\ T_{4,y} \\ T_{5,y} \end{bmatrix} = \begin{bmatrix} r_{21} \\ r_{23} \\ y_r \end{bmatrix}\right)\left(R_3 = M^{+} \begin{bmatrix} T_{1,z} \\ T_{2,z} \\ T_{3,z} \\ T_{4,z} \\ T_{5,z} \end{bmatrix} = \begin{bmatrix} r_{31} \\ r_{33} \\ z_r \end{bmatrix}\right) \\ M^{+} = \left(M^T M^{-1}\right)^{-1} \cdot M^T \end{cases} \tag{17}$$

$$\boldsymbol{V}_1 = \begin{bmatrix} r_{11} \\ r_{21} \\ r_{31} \end{bmatrix} \quad \boldsymbol{V}_3 = \begin{bmatrix} r_{13} \\ r_{23} \\ r_{33} \end{bmatrix} \quad \boldsymbol{V}_2 = \begin{bmatrix} r_{11} \\ r_{21} \\ r_{31} \end{bmatrix} \times \begin{bmatrix} r_{13} \\ r_{23} \\ r_{33} \end{bmatrix} = \begin{bmatrix} r_{12} \\ r_{22} \\ r_{23} \end{bmatrix} \tag{18}$$

In (17), M^{+} represents the pseudoinverse (Moore-Penrose inverse) of M. Based on the properties of rotation matrices, we determine that the cross products of the row vectors conform to the right-hand rule, thereby obtaining the relationships among V1, V2, and V3 in (18). Through precise calculations using five calibration points, we derive the optimal

approximate solution. In (19), $r_{ij}(i,j=1,2,3)$ and $x_r y_r z_r$ are variables used to record the results. Subsequently, the variables are normalized.

$$\hat{r}_{ij} = \frac{r_{ij}}{\sqrt{\sum_{i=1}^{3} r_{ij}^2}} (j = 1,2,3) \tag{19}$$

The calibration result matrix X is constructed, which is the required CHT^{-1}.

$$X = \begin{bmatrix} \hat{r_{11}} & \hat{r_{12}} & \hat{r_{13}} & t_x \\ \hat{r_{21}} & \hat{r_{22}} & \hat{r_{23}} & t_y \\ \hat{r_{31}} & \hat{r_{32}} & \hat{r_{33}} & t_z \\ 0 & 0 & 0 & 1 \end{bmatrix} \tag{20}$$

For any measurement point $\boldsymbol{P}$ with coordinates $\boldsymbol{p(u_0, v_0)}$, it is homogenized to obtain Equation (21).

$$p_{\{B\}} = BHT \quad \cdot \quad CHT^{-1} \cdot p = R \cdot X \cdot \begin{bmatrix} u_0 \\ 0 \\ v_0 \\ 1 \end{bmatrix} = \begin{bmatrix} x_0 \\ y_0 \\ z_0 \\ 1 \end{bmatrix} \tag{21}$$

The sensor performs repeated emission scanning of laser beams, calculates the time difference and angles of the round trip, and integrates the data to form a more comprehensive two-dimensional data image. Using Equation (21), any two-dimensional coordinate $p(u_0\,, v_0)$ can be converted into a three-dimensional coordinate $p(x_0\,, y_0\,, z_0)$, facilitating further point cloud construction.

In practical operation, the calibration object is placed under the robotic arm's world coordinate system within the working conditions. A central point and marking points in the four quadrants at different positions within the sensor's visual range are specified and extracted. As shown in Figure 21a, when adjusting the central point, the laser locator is activated to initiate origin position calibration. The laser beam is superimposed with the positioning beam along the Z and Y axes to obtain the central positioning point. When selecting the four quadrant marking points, refer to the visual range in Figure 21b. The sensor's field of view divisions and values are as follows: AB is the sensor's blind zone, BC is the sensor's positive range, CD is the sensor's negative range, BD is the sensor's effective range, C is the sensor's zero point, W1 is the near measurement end, and W is the far measurement end. All dimensions are in millimeters (mm).

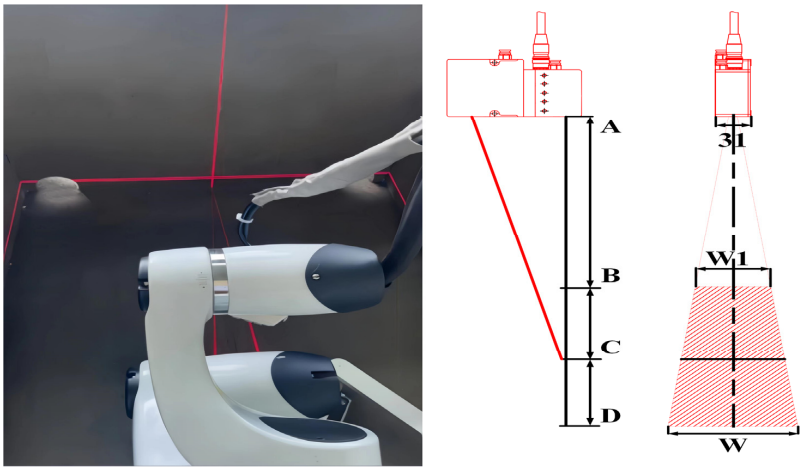

(**a**) (**b**)

Figure 21. Vision sensor calibration diagram. (**a**) Laser origin positioning calibration diagram. (**b**) Laser field distance dimensions.

During the process of selecting calibration point data, the four quadrant points should be chosen at optimal distances within the Z/Y axis data intervals specified by the laser's visual range. Based on the above processing rules, the calibration object is sequentially scanned at the four marking points. The calibration results are then subjected to precision estimation and comprehensive evaluation, and the data are recorded. The calibration result is shown in Figure 22.

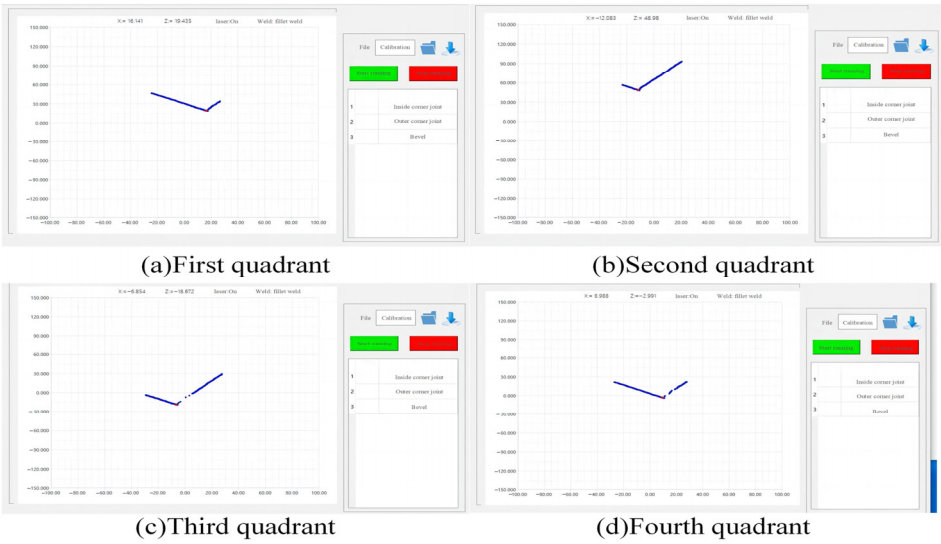

Figure 22. Calibration result graph.

3.2. Simulation Analysis of the Robotic Arm

3.2.1. Kinematic Analysis of the Robotic Arm

This six-degree-of-freedom robotic arm satisfies the Pieper criterion; this configuration has a closed-form solution. The main components of this robotic arm include the base, the upper and lower arms, the degrees-of-freedom joint modules (J1–J6), the tool flange, and communication and power cables. Each joint axis of the robotic arm is equipped with an independent servo motor and encoder, as shown in Figure 23, which illustrates the structural composition of the robotic arm body.

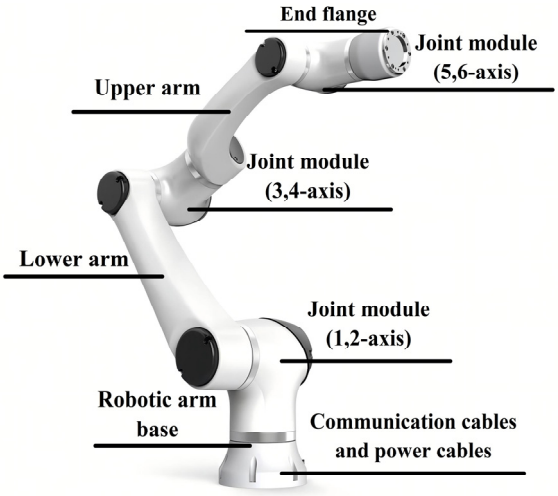

Figure 23. Structural diagram of the robotic arm body.

The kinematic model of the robotic arm is established using the standard D-H modeling method (standard Denavit-Hartenberg) [22]. The D-H parameters of this six-axis

welding robotic arm are shown in Table 6, and the coordinate system model established is depicted in Figure 24.

Table 6. Six-axis welding robotic arm D-H parameters.

Connecting Rod i	Torsional Angle α_i/°	Connecting Rod Length a_i/mm	Articular Angle θ_i/°	Offset Distance d_i/mm	Range of Joint Variables J_i/°
1	90	0	$\theta_1(0°)$	192.5	−360°~360°
2	0	266	$\theta_2(90°)$	0	−135°~135°
3	90	0	$\theta_3(90°)$	0	−150°~150°
4	−90	0	$\theta_4(0°)$	324	−360°~360°
5	90	0	$\theta_5(0°)$	0	−147°~147°
6	0	0	$\theta_6(0°)$	156.5	−360°~360°

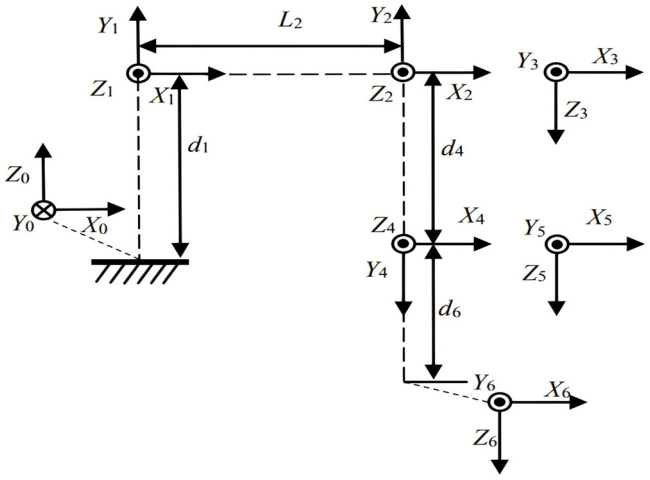

Figure 24. D-H coordinate system model diagram.

This experiment employs both analytical and iterative methods for analysis and solution. The analytical method combines algebraic and geometric approaches. The overall process of kinematic analysis is illustrated in Figure 25.

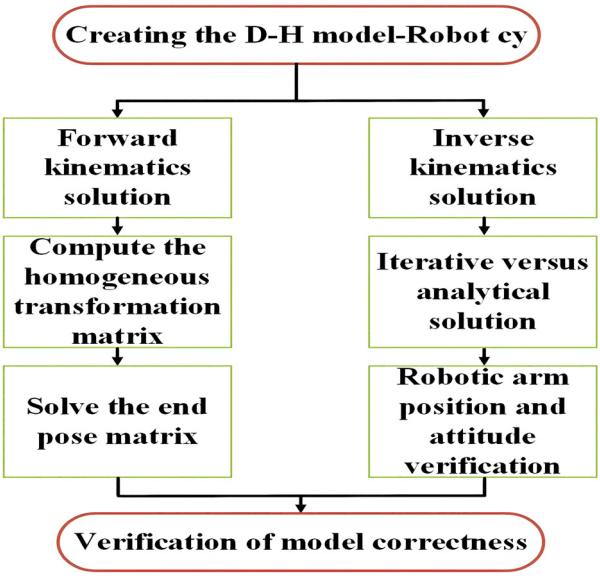

Figure 25. Kinematic analysis flow chart.

The forward kinematics equations express the transformation process between the base coordinate system at the origin of the robotic arm and the end-effector coordinate system using matrix T;

$$^{i-1}T = Rot(z,\theta_i) \times Trans(z,d_i) \times Trans(x,a_i) \times Rot(x,\alpha_i) \tag{22}$$

By expanding Equation (22), we obtain (23):

$$^{i-1}_{i}T = \begin{bmatrix} \cos\theta_i & -\sin\theta_i\cos\alpha_i & -\sin\theta_i\cos\alpha_i & a_i\cos\theta_i \\ \sin\theta_i & \cos\theta_i\cos\alpha_i & -\cos\theta_i\sin\alpha_i & a_i\sin\theta_i \\ 0 & \sin\alpha_i & \cos\alpha_i & d_i \\ 0 & 0 & 0 & 1 \end{bmatrix} \tag{23}$$

The homogeneous transformation matrix is shown in (24):

$$\begin{aligned} ^{0}_{1}T &= \begin{bmatrix} C_1 & 0 & S_1 & 0 \\ S_1 & 0 & -C_1 & 0 \\ 0 & 1 & 0 & d_1 \\ 0 & 0 & 0 & 1 \end{bmatrix} & ^{1}_{2}T &= \begin{bmatrix} C_2 & -S_2 & 0 & a_2C_2 \\ S_2 & C_2 & 0 & a_2S_2 \\ 0 & 0 & 1 & 0 \\ 0 & 0 & 0 & 1 \end{bmatrix} \\ ^{2}_{3}T &= \begin{bmatrix} C_3 & 0 & S_3 & 0 \\ S_3 & 0 & -C_3 & 0 \\ 0 & 1 & 0 & 0 \\ 0 & 0 & 0 & 1 \end{bmatrix} & ^{3}_{4}T &= \begin{bmatrix} C_4 & 0 & -S_4 & 0 \\ S_4 & 0 & C_4 & 0 \\ 0 & -1 & 0 & d_4 \\ 0 & 0 & 0 & 1 \end{bmatrix} \\ ^{4}_{5}T &= \begin{bmatrix} C_5 & 0 & S_5 & 0 \\ S_5 & 0 & -C_5 & 0 \\ 0 & 1 & 0 & 0 \\ 0 & 0 & 0 & 1 \end{bmatrix} & ^{5}_{6}T &= \begin{bmatrix} C_6 & -S_6 & 0 & 0 \\ S_6 & C_6 & 0 & 0 \\ 0 & -1 & 0 & d_6 \\ 0 & 0 & 0 & 1 \end{bmatrix} \end{aligned} \tag{24}$$

By sequentially multiplying the homogeneous transformation matrices, we obtain the following end-effector pose matrix (25):

$$^{0}_{6}T = {}^{0}_{1}T \cdot {}^{1}_{2}T \cdot {}^{2}_{3}T \cdot {}^{3}_{4}T \cdot {}^{4}_{5}T \cdot {}^{5}_{6}T = \begin{bmatrix} n_x & o_x & a_x & p_x \\ n_y & o_y & a_y & p_y \\ n_z & o_z & a_z & p_z \\ 0 & 0 & 0 & 1 \end{bmatrix} \tag{25}$$

In Equation (22), $Rot(z,\theta_i)$ and $Rot(x,\alpha_i)$ represent the transformation matrices for rotations about the Z and X axes by certain joint angles, respectively. $Trans(z,d_i)$ and $Trans(x,\alpha_i)$ represent the transformation matrices for translations along the Z and X axes by certain distances, respectively. In Equation (25), p_x, p_y, and p_z are spatial vectors that indicate the position of the robotic arm along the X, Y, and Z axes in space, forming spatial coordinate points. By expanding and solving the above analytical equations, we obtain the unique solution (26):

$$^{0}_{6}T = \begin{bmatrix} -1 & 0 & 0 & 0 \\ 0 & -1 & 0 & 0 \\ 0 & 0 & 1 & 939 \\ 0 & 0 & 0 & 1 \end{bmatrix} \tag{26}$$

To solve the inverse kinematics, the method of separating variables is employed. Both sides of the equation are multiplied by the inverses of the corresponding matrices to compute the solutions. The solved joint angles $\theta_1 - \theta_6$ are (30°, 30°, 45°, 45°, 60°, 60°), and the solutions are shown in Table 7.

Table 7. Inverse kinematics solution details.

Serial Number	$\theta_1/^\circ$	$\theta_2/^\circ$	$\theta_3/^\circ$	$\theta_4/^\circ$	$\theta_5/^\circ$	$\theta_6/^\circ$
1	30	30	45	45	60	60
2	30	−60	−45	−135	−60	−120
3	30	−109.6	45	76.84	38.96	13.29
4	30	−109.6	45	−103.16	−38.96	−166.7
5	−150	−250.3	−45	76.84	−38.96	−166.7
6	−150	−250.3	−45	−103.16	−38.96	13.29
7	−150	60	45	45	−60	−120
8	−150	60	45	−135	60	60

Discarding inaccurate solutions, we select the optimal solution that best fits the robotic arm's pose, which is the first set of solutions.

Another method for obtaining the inverse solution is the Newton-Raphson iterative method. First, we establish the nonlinear kinematic equations as shown in (27):

$$F(x) = f(x) - P_d = 0 \tag{27}$$

In Equation (27), $f(x)$ represents the forward kinematics of the robotic arm, and P_d represents the desired pose of the end effector. Let $\mathbf{r}$ be the root of $F(x) = 0$, and x_0 is chosen as the initial approximation of $\mathbf{r}$. By drawing the tangent line $\mathbf{L}$ to the curve $y = f(x)$ at the point $(x_0, f(x_0))$, which intersects the x-axis, we obtain the tangent Equation (28):

$$y = f(x_0) + f'(x_0)(x - x_0) \tag{28}$$

The intersection point x_1 with the x-axis is calculated, and then subsequent intersection points are iteratively found until the value approaches zero. The iterative formula for the k-th iteration is given by the following Equation (29):

$$x_{k+1} = x_k - \frac{F(x_k)}{F'(x_k)} \tag{29}$$

In Equation (29), $F'(x_k)$ represents the Jacobian matrix of the equation. In MATLAB 2022a, the maximum number of iteration steps and the error threshold are defined, and the current joint angles are set as the initial iteration angles to obtain a nonlinear twelve-dimensional error equation set. Running the iteration of Equation (29) computes the next joint angles and updates the nonlinear equations; the while loop exits when the maximum number of iterations is reached. The transformed Equation (25) is expressed as Equation (30):

$${}^0_6T = {}^0_1T{}^1_2T{}^2_3T{}^3_4T{}^4_5T{}^5_6T = \begin{pmatrix} {}^0_6R & {}^0_6P \\ 0 & 1 \end{pmatrix} \tag{30}$$

In Equation (30), ${}^0_6R$, and ${}^0_6P$ represent the rotational component and positional component of the robotic arm's end-effector pose relative to the base, respectively. They are used to construct twelve-dimensional nonlinear equations of forward kinematics. The Jacobian matrix is constructed as shown in Equation (31):

$$Jaco = \begin{bmatrix} \frac{\delta p_x}{\delta \theta_1} & \frac{\delta p_x}{\delta \theta_2} & \cdots & \frac{\delta p_x}{\delta \theta_6} \\ \frac{\delta p_y}{\delta \theta_1} & \frac{\delta p_y}{\delta \theta_2} & \cdots & \frac{\delta p_y}{\delta \theta_6} \\ \frac{\delta p_z}{\delta \theta_1} & \frac{\delta p_z}{\delta \theta_2} & \cdots & \frac{\delta p_z}{\delta \theta_6} \\ \frac{\delta r_1}{\delta \theta_1} & \frac{\delta r_1}{\delta \theta_2} & \cdots & \frac{\delta r_1}{\delta \theta_6} \\ \vdots & \vdots & \cdots & \vdots \\ \frac{\delta r_9}{\delta \theta_1} & \frac{\delta r_9}{\delta \theta_2} & \cdots & \frac{\delta r_9}{\delta \theta_6} \end{bmatrix} \tag{31}$$

The above method uses the Newton iterative formula to solve the inverse kinematics of the robotic arm; alternatively, it can be solved using the SVD method, which is a computational method for finding the pseudoinverse of a non-square matrix, as shown in Equation (32):

$$\begin{aligned} f_{\theta_d} &= \left[p_{x_d}, p_{y_d}, p_{z_d}, (r_1, r_2, r_3, r_4, r_5, r_6, r_7, r_8, r_9)_d\right]^T \\ f_{\theta_{n-1}} &= \left[p_{x_{n-1}}, p_{y_{n-1}}, p_{z_{n-1}}, (r_1, r_2, r_3, r_4, r_5, r_6, r_7, r_8, r_9)_{n-1}\right]^T \\ \theta_n &= \theta_{n-1} + SVD(Jaco(\theta_{n-1}))(f_{\theta_d} - f_{\theta_{n-1}}) \end{aligned} \tag{32}$$

After the kinematic solution of the robotic arm is completed, MATLAB Robotics Toolbox 10.4 is used to verify the robotic arm's postures. Four sets of experimental postures are selected. The joint variable values are $[pi/4,\ pi/4, pi/3, pi/3, pi/6, pi/6]$, $[pi/2, pi/4, pi/2, pi/4, pi/3, pi/3]$, $[0, pi/2, pi/6, 0, pi/2, pi/6]$. The corresponding forward kinematic end-effector pose matrices T1, T2, T3, T4 and the inverse kinematic solutions with corresponding joint angle values and pose matrices Ta, Tb, Tc, Td are obtained as shown below, where the fourth set of posture is the DH model diagram of the initial posture when the rail-mounted robotic arm starts, as seen in Figure 26.

$$T_1 = \begin{bmatrix} -0.9212 & -0.3066 & 0.2396 & 487.62 \\ 0.3509 & -0.3887 & 0.8519 & 391.79 \\ -0.1681 & 0.8689 & 0.4656 & 537.32 \\ 0 & 0 & 0 & 1 \end{bmatrix} \quad T_2 = \begin{bmatrix} -0.7891 & 0.0474 & -0.6124 & -95.8363 \\ -0.0018 & -0.9968 & -0.0795 & 404.7576 \\ -0.6142 & -0.0638 & 0.7866 & 732.7906 \\ 0 & 0 & 0 & 1 \end{bmatrix}$$

$$T_3 = \begin{bmatrix} 0.75 & 0.433 & 0.5 & 358.842 \\ 0.5 & -0.866 & 0 & 0 \\ 0.433 & 0.25 & -0.866 & 484.967 \\ 0 & 0 & 0 & 1 \end{bmatrix} \quad T_4 = \begin{bmatrix} 1 & 0 & 0 & -383.5 \\ 0 & 1 & 0 & 0 \\ 0 & 0 & 1 & 386.9 \\ 0 & 0 & 0 & 1 \end{bmatrix} \tag{33}$$

$$T_a : \theta_1 \sim \theta_6 : (45°, 45°, 60°, 60°, 30°, 30°) \quad T_b : \theta_1 \sim \theta_6 : (90°, 45°, 90°, 45°, 60°, 60°)$$
$$T_c : \theta_1 \sim \theta_6 : (0°, 90°, 30°, 0°, 90°, 30°) \quad T_d : \theta_1 \sim \theta_6 : (0°, -120°, 120°, -180°, 90°, 0°)$$

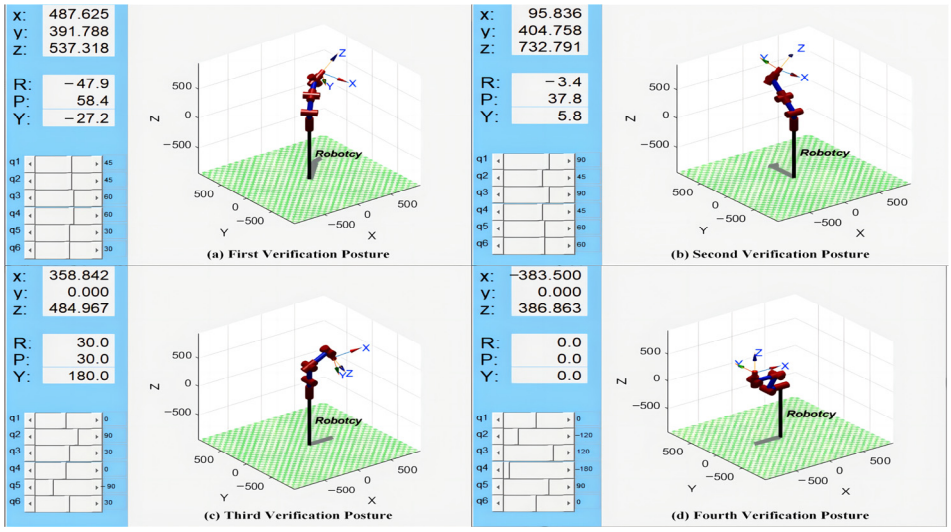

Figure 26. Robotic arm attitude verification diagram.

At this point, the calculation of experimental data within the effective variable ranges of joint angles for four sets of six-axis welding robotic arms has been completed. The output corresponding postures and joint angles have been verified, further confirming the correctness of the model and calculations, providing support for subsequent simulation work [23].

3.2.2. Trajectory Planning of the Robotic Arm

Many scholars at home and abroad have proposed path planning methods [24] and trajectory optimization methods [25] for welding robotic arms, but comparative analyses are rare. This experiment conducts comparative analyses of unoptimized trajectories, uniform speed processing, cubic interpolation, and quintic interpolation trajectory planning algorithms, applying constraints on the joint axis velocities and accelerations of the robotic arm during the planning process. The specific flowchart is shown in Figure 27.

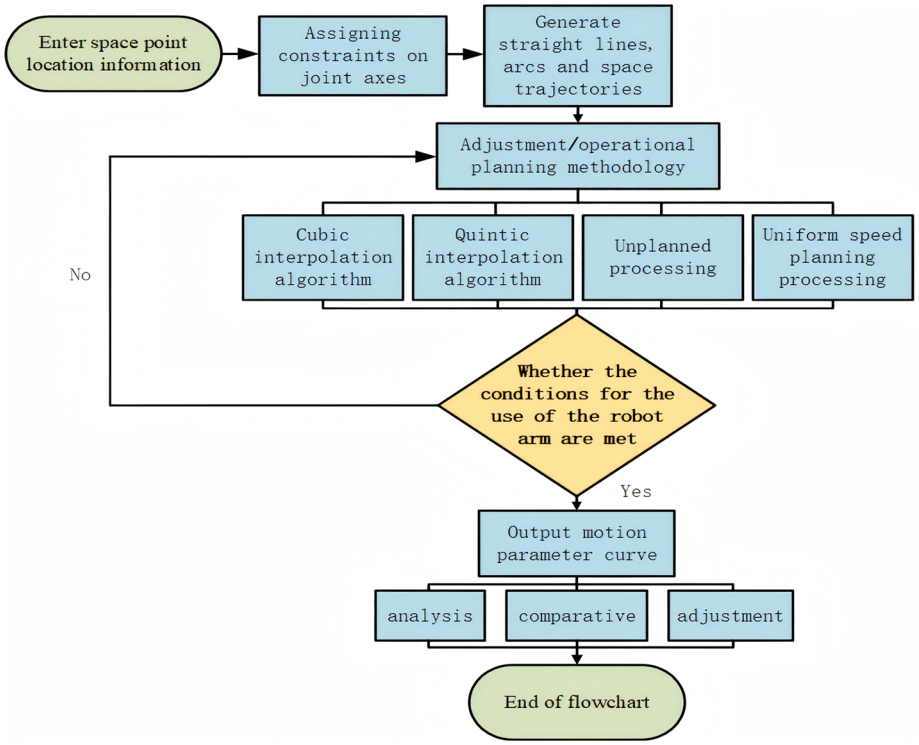

Figure 27. Trajectory planning flow chart.

The simulation time is 2 s, with initial and terminal angular velocities of 0. The starting point is (−200, 200, −50), the guiding point is (−150, 100, −100), and the terminal point is (−200, −50, 75). The number of sampling points is 50. The initial joint radian values are (2.3171, 2.3171, 2.4888, −1.6219, −2.2184, 0), and the terminal joint radian values are (−0.2202, −0.2202, 2.0665, −0.1613, 2.7961, 0). The expressions for cubic and quintic polynomial interpolation functions are shown in Equations (34) and (36):

$$q_{(t)} = a_0 + a_1(t - t_0) + a_2(t - t_0)^2 + a_3(t - t_0)^3 \tag{34}$$

Equation (35) is the calculation formula for the four constant parameters in the cubic interpolation polynomial:

$$\begin{cases} a_0 = q_0, a_2 = \frac{1}{T^2}[3h - (v_1 + 2v_0)T] \\ a_1 = v_0, a_3 = \frac{1}{T^3}[-2h + (v_1 + v_0)T] \end{cases} \tag{35}$$

$$\theta_t = \theta_0 + a_1(t - t_0) + a_2(t - t_0)^2 + a_3(t - t_0)^3 + a_4(t - t_0)^4 + a_5(t - t_0)^5 \tag{36}$$

Equation (37) is the calculation formula for the six constant parameters in the quintic interpolation polynomial:

$$\begin{cases} a_0 = \theta_0, a_3 = \frac{1}{2T^3}[20h - (8v_1 + 12v_0)T - (3a_0 - a_1)T^2] \\ a_1 = v_0, a_4 = \frac{1}{2T^4}[-30h + (14v_1 + 16v_0)T - (3a_0 - 2a_1)T^2] \\ a_2 = \frac{1}{2}a_0, a_5 = \frac{1}{2T^5}[12h - 6(v_1 + v_0)T + (a_1 - a_0)T^2] \end{cases} \tag{37}$$

In Equations (35) and (37), v_0 represents the initial joint velocity, v_1 is the final joint velocity, a_0 is the initial joint acceleration, a_1 is the final joint acceleration, $T = t_1 - t_0$, $h = q_1 - \theta_0$, θ_0 is the initial joint angle, and q_1 is the final joint angle. After running the analysis and comparison, the trajectory planning effects are contrasted as shown in Figure 28.

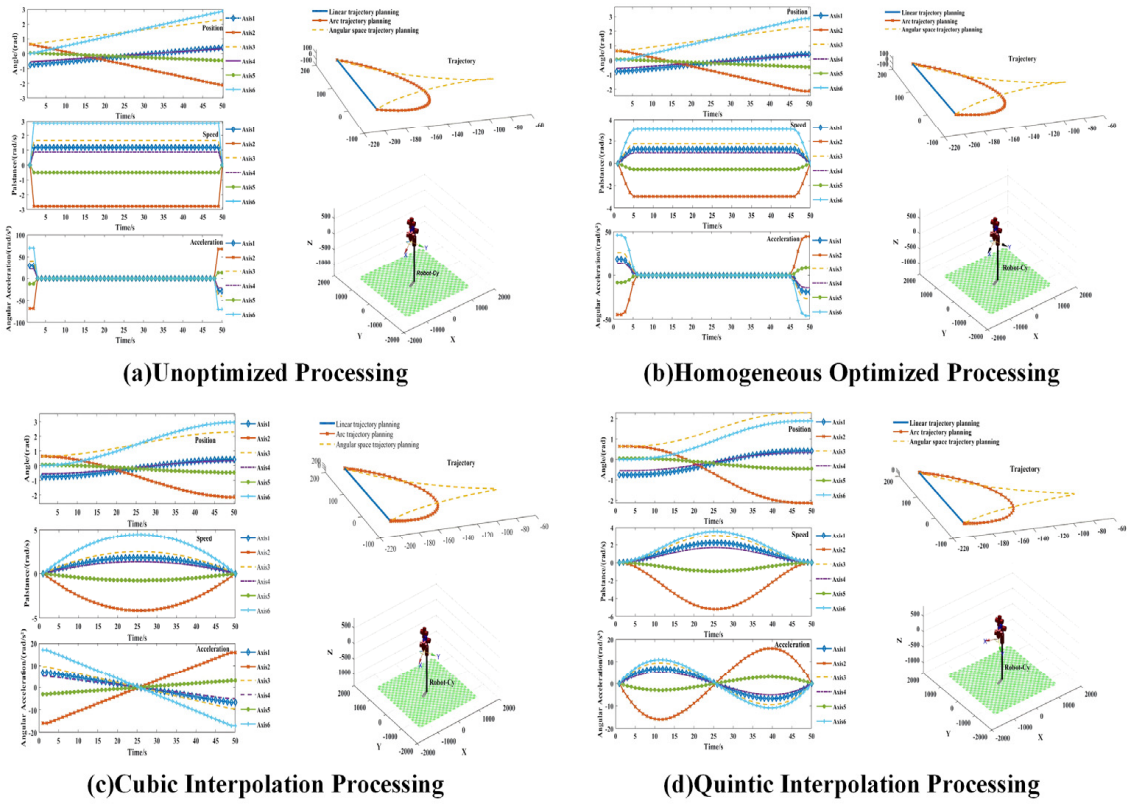

Figure 28. Comparative analysis chart for trajectory planning.

Completing this comparative analysis study can provide practical assistance for the formulation of subsequent processing strategies. As seen from Figure 28, cubic interpolation achieves smooth operation of the joint axes, while quintic interpolation yields even better results. In the future, multi-robot-arm cooperative trajectory planning and obstacle avoidance can be developed to further enhance the automation and intelligence levels of welding robotic arms [26].

3.2.3. Workspace Analysis of the Robotic Arm

In this section, the Monte Carlo method is used to calculate the robotic arm's global workspace and the constrained workspace analysis that fits the actual working conditions and processing requirements, respectively. The specific workflow is shown in Figure 29.

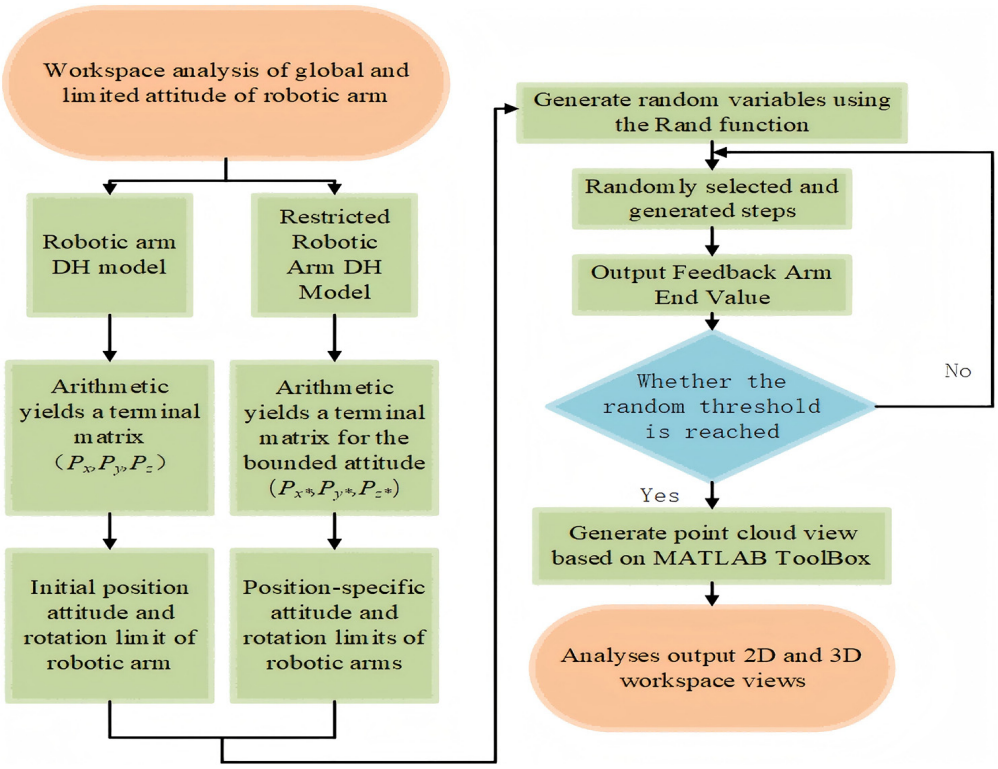

Figure 29. Workspace solution analysis diagram.

First, the spatial position vector of the end effector is obtained from the forward kinematics equations, and the position vector (38) is derived from the end pose matrix in Equation (30).

$$p = \begin{bmatrix} p_x \\ p_y \\ p_z \end{bmatrix} = \begin{bmatrix} D_3(S_5(S_1S_4 + C_4(C_1C_{23})) + C_5(C_1S_{23}) + D_2(C_1S_{23}) - A_2C_1C_2 \\ D_2S_1S_3(C_2 + C_4(C_{23})) - C_5S_1(S_{23})) - A_2C_2S_1 \\ D_1 - D_3(C_5C_{23}) - C_4S_5(S_{23}) - D_2C_{23} - A_2S_2 \end{bmatrix} \quad (38)$$

The number of sample points is set to N = 5000. In the MATLAB environment, the Rand function is used to define uniform random numbers in (0, 1), generating random step sizes L:

$$L = \left(q_i^{max} - q_i^{min}\right) \times Rand(N, 1) \quad (39)$$

The random variable is (40):

$$q_i = q_i^{min} + \left(q_i^{max} - q_i^{min}\right) \times Rand(N, 1) \quad (40)$$

In Equation (40), q_i^{max} and q_i^{min} represent the maximum and minimum rotation limits of joint i of the robotic arm, respectively, where $i = 1 \sim 6$. The iterative execution steps are repeated according to the number of samples until the maximum number of random samples is reached. MATLAB outputs the point cloud diagram of the robotic arm's workspace based on the collected points. Figure 30a is the DH model of the initial working posture of the robotic arm; in Figure 30b, the coordinate system is the reference coordinate system, and the center point of the robotic arm base is the origin coordinate system. Figure 30c,d are the robotic arm welding posture diagrams.

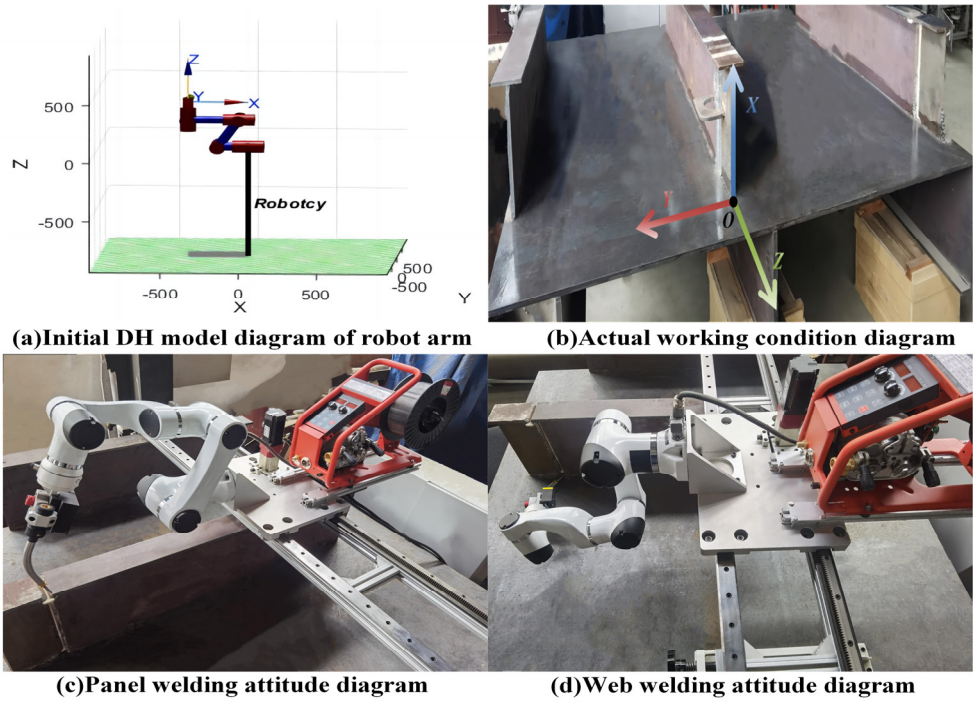

(a)Initial DH model diagram of robot arm (b)Actual working condition diagram

(c)Panel welding attitude diagram (d)Web welding attitude diagram

Figure 30. Working condition and robotic arm posture information diagram.

The global experimental parameters for the robotic arm workspace analysis and the experimental parameters for the constrained welding postures within the working conditions are shown in Tables 8 and 9, respectively. The dimensions of the workspace point clouds for both are listed in Table 10. The output two-dimensional and three-dimensional point cloud views are shown in Figure 31.

Table 8. Global experimental parameters of robotic arm.

Serial Number	Experimental Information	Unit/(mm)
1	Working arm span (Robotic arm)	590 mm
2	Erection height (Track)	540 mm
3	Erection length (Track)	2030 mm
4	Welding posture (panel)	(0°, 22.14°, 114°, −180°, −71.1°, 58.26°)
5	Welding position (panel)	(−185.77, −54.39, 535.38, 86.18, 77.88, −85.64, U(316.43))
6	Welding posture (vertical plate)	(−156°, −78.1°, 42.8°, −257.7°, −98.4°, −148.4°)
7	Welding position (vertical plate)	(−440.76, 299.82, 582.54, 20.14, 128.22, 106.42, U(−96.96))

Table 9. Experimental parameters of the confined robotic arm welding attitude.

Serial Number	Working Position	Position and Attitude Information (World Coordinates)
1	Robotic arm base position	$(540, -425, 675)$
2	Initial working position and attitude	J1 $\sim$ J6; $(0°, -120°, 120°, -180°, 90°, 0°)\begin{pmatrix} -712.22, -81.86, 370.22, \\ -123.03, 112.8, 29.8, U(-93.69) \end{pmatrix}$
3	Panel	Initial coordinate: $\begin{pmatrix} -187.82, -52.18, 536.091 \\ 85.17, 77.78, -84.21, U(314.69) \end{pmatrix}$ Initial posture: J1 $\sim$ J6; $\begin{pmatrix} 0°, -121.1°, 113.5°, \\ -180°, -70.7°, -300.2° \end{pmatrix}$ Termination coordinate: $\begin{pmatrix} -185, 45.05, 538.1, 85.18 \\ , 80.95, -84.47, U(314.69) \end{pmatrix}$ Discontinuance posture: J1 $\sim$ J6; $\begin{pmatrix} 20°, -126°, 114°, \\ -161.5°, -71.15°, -295.85° \end{pmatrix}$

Table 9. *Cont.*

Serial Number	Working Position	Position and Attitude Information (World Coordinates)
4	Vertical plate	Initial coordinate: $\begin{pmatrix} -520.04,\ 408.88,\ 548.67, \\ 9.77,\ 64.46, -83.27, \mathrm{U}(-96.95) \end{pmatrix}$ Initial posture: J1 $\sim$ J6; $\begin{pmatrix} -172.6^\circ, -91.8^\circ, -77.1^\circ, \\ -273.7^\circ, -75^\circ, 44.5^\circ \end{pmatrix}$ Termination coordinate: $\begin{pmatrix} -191.72,\ 399.52,\ 535.9, \\ -2.64, 68.1, -63.66, \mathrm{U}(-96.95) \end{pmatrix}$ Discontinuance posture: J1 $\sim$ J6; $\begin{pmatrix} 121.58^\circ, -80.86^\circ, 116.47^\circ, \\ -239.83^\circ, -54.49^\circ, -109.53^\circ \end{pmatrix}$

Table 10. Point cloud data in the workspace.

Analysis Type	Position	Articular Angle: $i_{(1\sim6)}$	Orientations	Point Cloud Size: Min~Max: (mm)
global analysis	panel	$i_1(-120\sim150^\circ)$ $i_2(-130\sim-30^\circ)$ $i_3(60\sim120^\circ)$ $i_4(-360\sim360^\circ)$ $i_5(-130\sim150^\circ)$ $i_6(-230\sim360^\circ)$	*X*-axis *Y*-axis *Z*-axis	−896.48~458.34 −735.09~739.48 −608.9~736.38
global analysis	vertical plate	$i_1(-170\sim110^\circ)$ $i_2(-135\sim-50^\circ)$ $i_3(5\sim90^\circ)$ $i_4(-270\sim-105^\circ)$ $i_5(-150\sim-75^\circ)$ $i_6(-285\sim-65^\circ)$	*X*-axis *Y*-axis *Z*-axis	−730.31~134.75 −615.09~620.32 −592.46~624.16
locality confined analysis	panel	$i_1(0\sim20^\circ)$ $i_2(-126\sim-115^\circ)$ $i_3(106\sim114^\circ)$ $i_4(-180\sim-161^\circ)$ $i_5(-71\sim-68^\circ)$ $i_6(-300\sim-290^\circ)$	*X*-axis *Y*-axis *Z*-axis	−477.81~−432.33 −46.72~65.53 97.93~216.65
locality confined analysis	vertical plate	$i_1(-174\sim-120^\circ)$ $i_2(-92\sim-75^\circ)$ $i_3(73\sim117^\circ)$ $i_4(-275\sim-238^\circ)$ $i_5(-75\sim-54^\circ)$ $i_6(-110\sim113^\circ)$	*X*-axis *Y*-axis *Z*-axis	−676.08~−486.34 −394.99~−43.88 −339.70~121.07

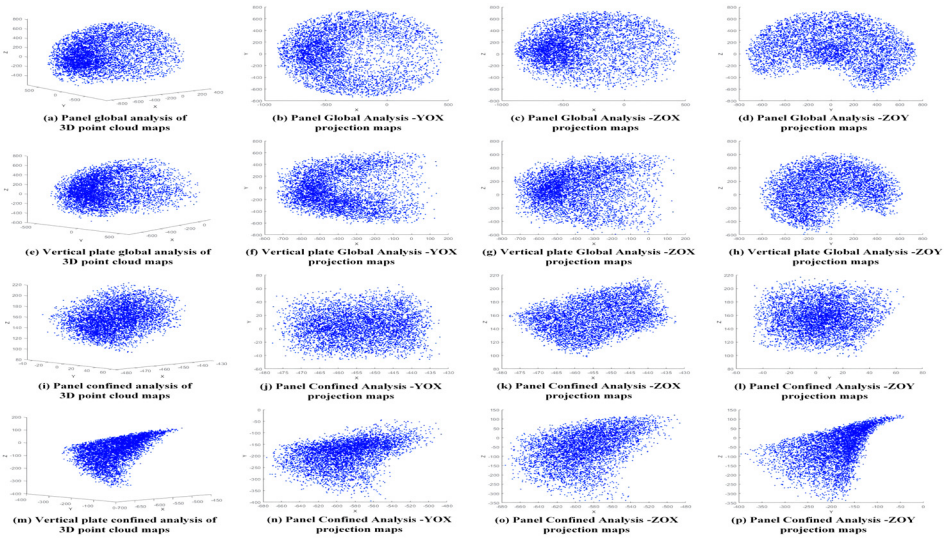

Figure 31. Work space point cloud data map.

Through the analysis of experimental results, it can be seen that this scheme can completely cover the welding parts required for this working condition.

4. Equipment Operation Testing and Visual Scanning Simulation

4.1. Analysis of Small Assembly Working Conditions

The material of the small assembly working condition is Q235-B steel, with length units in millimeters. The length and width of the bottom plate of the small assembly are both 1800 mm. The assembly, from left to right, has bottom edge lengths of 1200 mm, 1350 mm, and 1350 mm. The thicknesses of the panel, web, and bottom plate are all 13 mm. The height of the web is 360 mm, and the width of the panel is 100 mm. The distances

between the assembly plates are 720 mm and 960 mm, respectively. The lug thickness is 13 mm, the chamfer is 20 mm, the empty ring radius is 40 mm, the length is 130 mm, and the width is 120 mm. Height 1 is 176.5 mm, which is the distance from the bottom surface of the lug to the upper surface of the bottom plate. Height 2 is 147.5 mm, which is the distance from the upper edge of the lug to the lower surface of the panel. The width of the web ceramic gasket is 30 mm, and the length is 360 mm. The panel ceramic gasket has a length of 360 mm and a width of 30 mm. Specific details are shown in Figure 32.

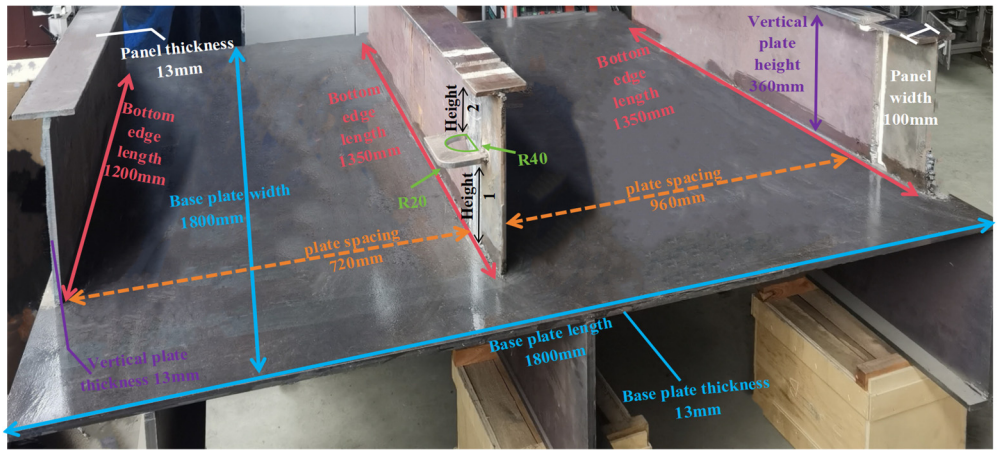

Figure 32. Small assembly plates working conditions.

4.2. Analysis of Groove Working Conditions

This section plans and analyzes the processing of the V-shaped butt groove of this plate. The specific groove sectional view and simulation diagram are shown in Figure 33a,b.

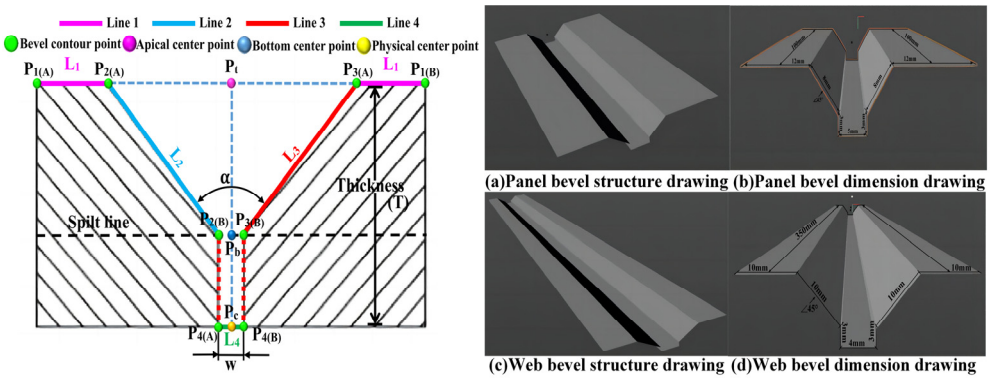

Figure 33. Cutaway view of plate butt bevel.

In Figure 33a, P_t, P_b, and P_c are the vertex of the center line of the plate groove, the midpoint of the division, and the bottom endpoint, respectively. P1–P4 are the endpoints of each plane; P(A) and P(B) are the left and right endpoints of the corresponding slope line segments. L1, L2, L3, and L4 are the sectional widths of planes 1 to 4; α is the angle of the butt groove; **w** is the distance range value between the left and right edge points at the bottom end of the groove; T is the overall thickness of the groove; the dashed line represents the division line between the butt groove and the ceramic backing. The groove parameters of the panel and web are shown in Table 11.

Welding is performed in the plane where L1 is located at the midline distance between L2 and L3. Both the panel and the web adopt multi-layer and multi-pass welding. The welding procedures include root welding, fill welding, and cap welding. The panel's welding preparation process consists of five layers and seven passes, while the web's welding preparation process consists of three layers and five passes. The welding method

uses FCAW-GA, and CO_2 is employed as the shielding gas. The start and end welding positions are set with run-on and run-off plates according to processing requirements.

Table 11. Plate butt bevel parameters.

Serial Number	Symbols	Numerical Values (Panel)	Numerical Values (Vertical Plate)
1	L1	6 mm	5 mm
2	L2	8 mm	10 mm
3	L3	8 mm	10 mm
4	L4	5 mm	4 mm
5	α	45°	45°
6	T	11 mm	13 mm

4.3. Equipment Operation Testing

In this section, the equipment was operated to perform working condition scanning tests, yielding the average operating speed of the equipment, the rated power errors of the robotic arm joints, TCP, and U-axis rail, and the positioning errors under full power. The specific experimental power range for the rail motor and robotic arm is (1500–6000) W. The robotic arm joint axes and TCP operate using world coordinates, with the robotic arm joint axes corresponding to their respective encoder values. When the external U-axis runs along the rail, the movement distance is recorded based on servo motor feedback. Through error analysis and operating speed analysis, the equipment test results meet the processing requirements for small assemblies, as shown in Figure 34. Figure 34a shows the equipment positioning error under the full power range; Figure 34b shows the equipment positioning error under the rated power range; Figure 34c shows the rail operating speed under rated power; and Figure 34d shows the robotic arm TCP operating speed under rated power.

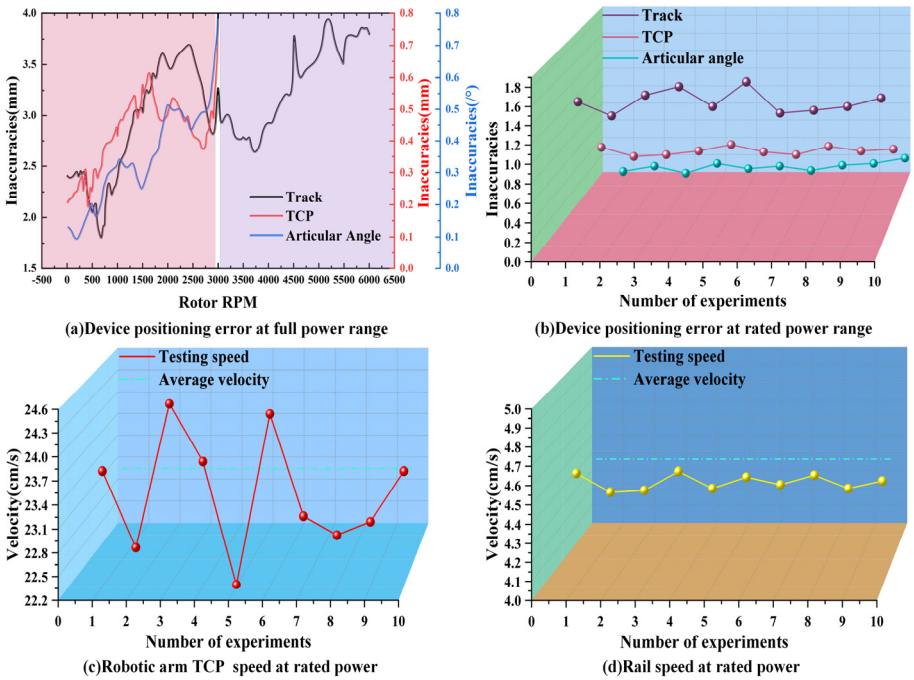

Figure 34. Equipment operation test chart.

4.4. Equipment Scanning Strategy

4.4.1. Scanning Trajectory and Spatial Poses

In terms of weld groove scanning strategies, some studies have proposed the multi-step method [27] and the smooth spline curve planning method [28] to extract weld features. Although these methods ensure operational precision, they can introduce a series of unpredictability for rail operations. This paper formulates a rail-based scanning strategy for the web and panel in small assembly working conditions, including the equipment's

scanning path, motion posture, weld groove information extraction, and point cloud processing. The technical parameters in the scanning strategy are detailed in Appendix A.

After completing the overall mechanical and communication connections of the equipment, the robotic arm is debugged to connect with the external axis, and automatic operation is initiated. The equipment first reaches the initial scanning position and posture at point 0 specified for the workpiece, then changes posture to reach point 1, which is located 390 mm in the Y-direction and 495 mm in the Z-direction from the Cartesian coordinate origin at the center of the robotic arm base. After the automatic welding equipment moves to the fixed position at point 2 via the external axis, the robotic arm adjusts its posture and position to points 3 through 6. This adjustment aligns the laser beam perpendicular to the *Z*-axis of the reference coordinate system, directing it onto the bottom plate of the workpiece and initiating the laser swing scanning mode. At this point, the external axis is temporarily fixed. This position and posture ensure that the robotic arm's TCP (tool center point) is not lower than the height of the base center point. Subsequently, the robotic arm moves along the *Z*-axis via the external axis to the sub-assembly panel while adjusting its posture to point 7. When the laser projects onto the panel, the operation stops, and the external axis is temporarily fixed. Meanwhile, the robotic arm adjusts its posture through points 8 to 10 to acquire the panel groove information and the plate height and dimension data.

After acquiring the information, the robotic arm moves back to the initial scanning position at point 7, then moves along the Z-direction via the external axis to locate point 11. Carrying the laser sensor, the robotic arm moves to the position with the most accurate viewing distance to obtain the bottom plate information of the workpiece and analyzes to calculate the distance between the panel and the robotic arm base. The robotic arm adjusts its posture and position to reach point 12, directing the laser sensor toward the side web of the workpiece, and analyzes to calculate the distance information between the robotic arm base and the sub-assembly side web. It then adjusts position and posture to make the laser beam parallel to the *Z*-axis of the reference coordinate system while moving to point 13, where it is completely parallel and coincides with the junction of the sub-assembly web and the bottom plate base surface within the workpiece. Scanning in the positive X-direction under the reference coordinate system, it extracts the entire sub-assembly groove web information and plate width data. At this point, the scanning ends and returns to point 0. For this workpiece, Figure 35 shows the TCP motion trajectory projection diagram of the laser sensor scanning process. Under the world coordinate system, there is no interference among the automatic welding equipment, robotic arm, external axis, and workpiece, and the laser sensor scanning viewing distance is optimal.

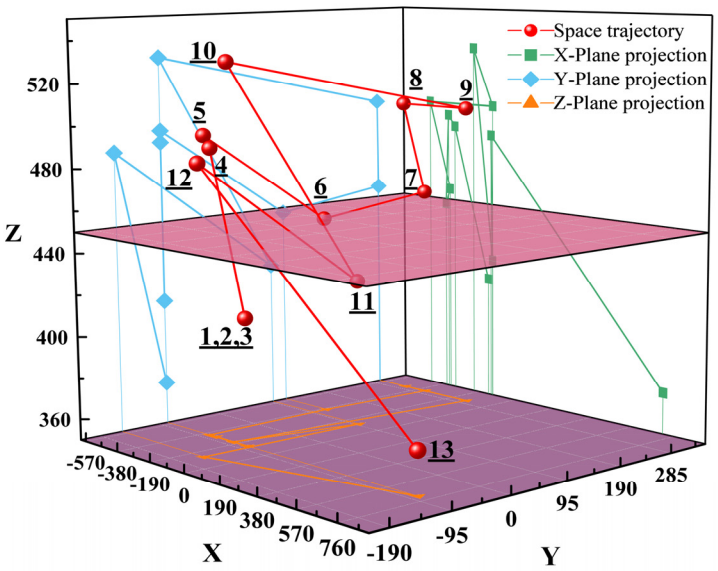

Figure 35. TCP motion trajectory projection.

4.4.2. Visual Scanning Processing of Grooves

In Figure 36a,b, the conditions for filtering the point cloud include point cloud intensity and size, variations in world coordinate positions, weld seam types and lap angles, and changes in planar dimensions. The scanned point clouds undergo further optimization and filtering. As shown in Figure 36b, each time the laser beam scans a groove, the acquired information contains N two-dimensional points. The sensor collaborates with the host computer to convert these two-dimensional pixel information points into three-dimensional spatial points. Figure 36c,d display the three-dimensional point clouds of the web and panel after applying the filtering conditions, featuring fewer noise points and exhibiting higher clarity and quality.

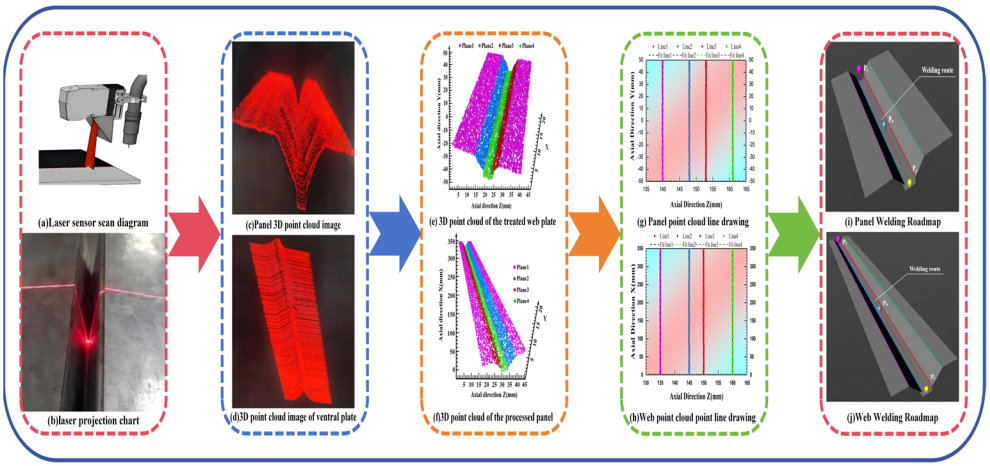

Figure 36. Bevel scanning and information processing flow chart.

Subsequently, the filtered three-dimensional point clouds are further processed. The host computer generates *Plane1* for the upper planes at both ends of the laser-scanned groove. It creates *Plane2* and *Plane3* for the inclined planes formed by the normal vectors of the two side slopes inside the groove. By analyzing the scanning information of the groove and calculating the height difference between the upper and lower end planes, the bottom plane *Plane4* is generated. As shown in Figure 36e,f, the final processed three-dimensional point clouds of the plate groove's web and panel are output.

Next, boundary conditions are set. Using an extremum algorithm, the edge point clouds at the intersections of *Planes 1* to *4* are extracted. The point clouds are then fitted into point-line diagrams utilizing the host computer's Visual Studio environment, the RANSAC (Random Sample Consensus) algorithm, and the least squares method. As illustrated in Figure 36g,h, four fitted dashed lines—*Fit line1* to *Fit line4*—are generated based on the extracted inner and outer contour lines *Line1* to *Line4* of the web groove and panel groove. Finally, the host computer evaluates the path line segments and computes the central value, outputting the welding path located at the center of the groove. This provides more precise operational assurance for the upcoming welding work, as shown in Figure 36i,j.

5. Multi-Layer and Multi-Pass Welding Experiments

5.1. Multi-Layer and Multi-Pass Welding Processes

After the point cloud features are extracted and fitted through the vision module, the development of multi-layer and multi-pass welding process strategies is immediately undertaken. This module is particularly important for intelligent welding operations [29]. In the welding experiments of the sub-assembly plate's web and panel using automatic welding equipment, the entire welding process is divided into the following four stages: welding preparation, pre-welding experiment, welding experiment, and post-welding experiment. The experimental flowchart of the rail-type multi-layer and multi-pass automatic welding equipment is shown in Figure 37.

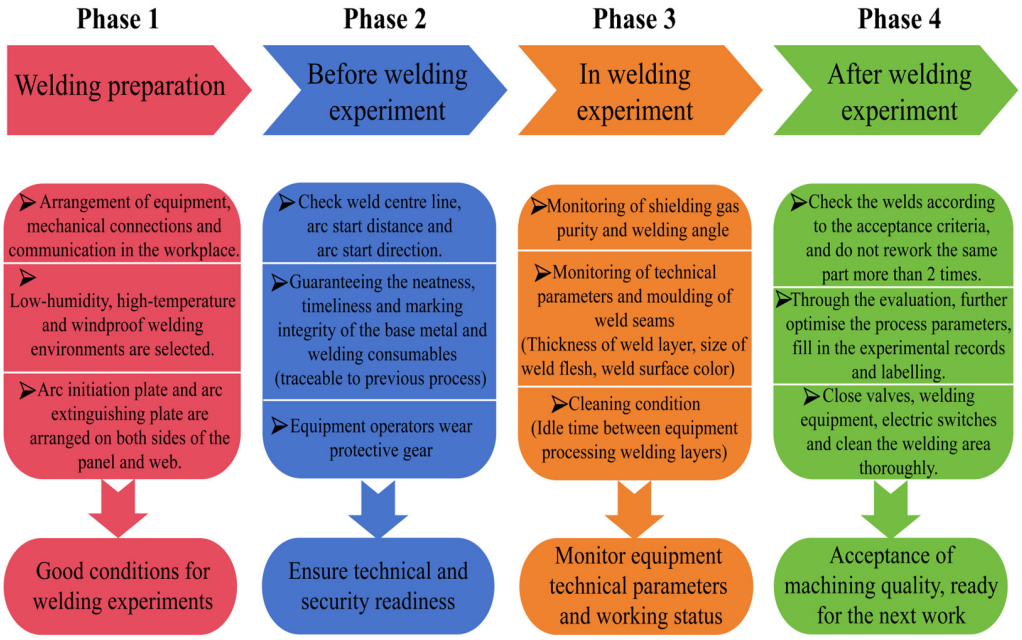

Figure 37. Welding experiment flow chart.

The experimental conditions for the rail-type automatic welding are listed in Table 12, and the detailed parameters of the multi-layer and multi-pass welding process for the plate's panel and web are shown in Table 13.

Table 12. Welding test conditions.

Serial Number	Working Condition	Panel	Vertical Plate
1	Plate material	Q235	Q235
2	Sheet specification	350 mm × 11 mm (blunt edge ≈ 1 mm)	100 mm × 18 mm (blunt edge ≈ 1 mm)
3	Welding wire parameters	Flux-Cored carbon steel welding wire (ϕ1.2) mm	Flux-Cored carbon steel welding wire (ϕ1.2) mm
4	Weld (layers, paths)	Three-layer, Four-pass	Five-layer, Seven-pass
5	Electrode connection mode	DCEP	DCEP
6	Welding position	1 G	3 G
7	Welding direction	Flat welding	Upward welding
8	Protective gas and flow	CO_2 (100%), 15–20 L/min	CO_2 (100%), 15–20 L/min
9	Wire feed speed	170 mm/min	170 mm/min
10	Average working speed	120 mm/min	135 mm/min

Table 13. Detailed parameters of the multi-layer multi-pass welding process for panels and vertical plates.

Position	Working Procedure	Layers	Passes	Welding Method	Amps/A	Voltage/V	Welding Speed/(mm/min)	Horizontal Swing Distance/mm	Corner Delay/ms
Panel	Underfill welding	1	1	FCAW-GA	190∼200	21.5∼27.5	107	1	300
	Filler welding	2	1	FCAW-GA	215∼225	24.5∼29	120	4	200
	Filler welding	3	1	FCAW-GA	215∼225	24.5∼29	120	5	300
	Filler welding	4	1	FCAW-GA	215∼225	24.5∼29	120	8	300
	Filler welding	4	2	FCAW-GA	215∼225	24.5∼29	120	8	300
	Cover welding	5	1	FCAW-GA	205∼215	23∼28	126	6	150
	Cover welding	5	2	FCAW-GA	205∼215	23∼28	126	6	150
vertical plate	Underfill welding	1	1	FCAW-GA	185∼200	22.5∼28.5	90	1~3	300
	Filler welding	2	1	FCAW-GA	210∼220	25∼30	150	6	100
	Filler welding	3	1	FCAW-GA	210∼220	24.5∼29.5	150	6	100
	Cover welding	3	2	FCAW-GA	205∼215	24.5∼29.5	150	7	100

5.2. Comparison of Welding Experiment Results and Benefits

Taking a single plate's web and panel multi-layer and multi-pass processing experiment as an example, a comparison is made between the rail-type automatic welding equipment and manual welding. The welding performance comparison analysis is shown in Figure 38. The data in Figure 38a,b include the overall weld seam formation rate of the sub-assembly plate's panel and web groove, welding material consumption, and welding efficiency. After ten experiments, the formation rate of the rail-type automatic welding equipment is stably higher than that of manual welding by 11.48%, the total material consumption is reduced by 13.4%, and the unit material consumption is reduced by 13.5%.

Figure 38. Welding performance comparative analysis diagram.

The comparative analysis results of the overall efficiency, production efficiency under working conditions, and processing costs between automatic welding and manual welding are shown in Table 14.

Table 14. Comparative analysis of welding performance.

Welding Method	Material Consumption (KG)	Unit Consumable (KG/M)	Ratio of Briquetting (%)	Number of Experiments
Automatic welding	1.7765	0.845	98.699	10
Manual welding	2.052	0.977	87.219	10

Under the same production conditions, following the data in the previous table, comparative experiments were conducted on sub-assembly panels and webs with different gaps using automatic welding and manual welding. From Table 15, it can be seen that when the gap is 4 mm, the efficiency increases by 7.35%, and time is saved by 10.2%; when the gap is 5 mm, the efficiency increases by 10.7%, and time is saved by 7.39%. Therefore, it can be concluded that automatic welding is more efficient than manual welding and also saves time costs.

Table 15. Sheet production efficiency comparative analysis table.

Welding Method	Number of Welding Paths	Clearance (*P*/mm)	Welding Time (t_1/min)	Readiness Time (t_2/min)	Auxiliary Time (t_3/min)	Total Time (t/min)	Production Efficiency (mm·min^{-1})
Automatic welding	7	4	9.33	30	11.5	50.83	17.14
	4	5	12.37	28	9.15	49.52	33.75
Manual welding	7	4	13.28	22	21.3	56.58	15.91
	4	5	15.47	24	14	53.47	30.5

Subsequently, as shown in Table 16, taking 1000 plates with the same specifications and processing conditions as the above single-plate experiment as an example, an economic benefit comparative analysis of the two processing methods was carried out. The total weld seam length is 450 m. In the analysis conditions, both the rail-type automatic welding equipment and manual welding are configured with two welders working in shifts, with a daily working time of 12 hours. Among them, the workers operating the automatic welding equipment are junior welders with a daily wage of 150 yuan, and the workers performing manual welding are senior welders with a daily wage of 230 yuan. From the analysis results in Table 16, it can be seen that the labor cost of automatic welding is reduced by 41.4% compared to manual welding, and 16.7% of the time cost is saved.

Table 16. Sheet production efficiency comparative analysis table.

Welding Method	Gross Production Efficiency (mm/min)	Total Welding Time (t_2/Day)	Welder's Expense (Yuan/Day^{-1})	Welding Material Cost (Yuan)	Total Cost (Yuan)
Automatic welding	11.45	55	8250	27,013	35,263
Manual welding	9.54	66	15,180	45,063	60,243

The schematic diagrams of the results for automatic welding and manual welding are shown in Figure 39a,c,e and Figure 39b,d,f, respectively. As seen in Figure 39, the weld seam appearance welded by the orbital automatic welding equipment is more uniform, with better consistency and minimal defects. The formation and coloration are aesthetically pleasing and meet the required standards. Table 17 provides a detailed comparative analysis of the welding effects between automatic and manual welding under the condition of a single workpiece. The labor and material costs in Table 17 include the labor and consumable costs for fully processing a single sheet of the test panel. Welding current and voltage can be freely selected within the given range according to the actual welding environment on site. Welding time includes both the welding operation time and the buffer time between each welding layer or pass. Further, as summarized from the above Table 14 to Table 17, it can be inferred from the CO_2 gas shielded multi-layer, multi-pass welding comparison experiments that automatic welding of the group-assembled plate will exhibit higher fatigue life compared to manual welding [30]. At the same time, it achieves the goals of reducing costs and improving efficiency. It also helps to some extent in relieving manual labor and reducing labor costs, consumable costs, and time wastage.

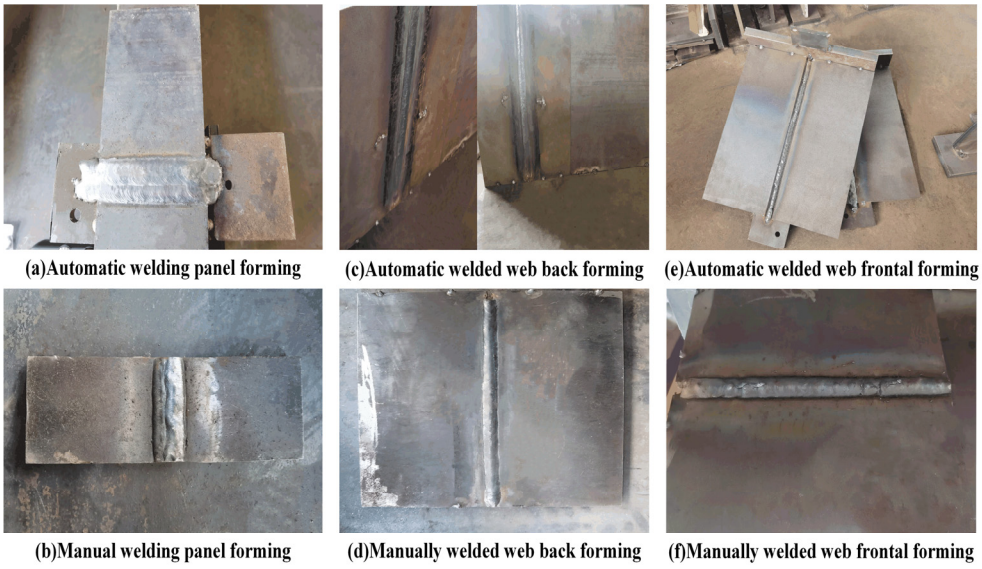

Figure 39. Schematic diagram of automatic and manual welding results.

Table 17. Detailed comparative analysis of welding effects for single sheet panels.

Welding Method	Types of Welding	Labor and Material Costs (Yuan)	Average Current/A	Average Voltage /V	Average Welding Speed (mm/min)	Welding Time (min)	Number of Defects
Automatic welding	CO_2 gas shielded welding	152.7	205∼215	24.5∼29.5	126	23.78	0
Manual welding	CO_2 gas shielded welding	234.5	195∼220	21∼30.5	120	27.41	2

The final welding process effect diagrams of the sub-assembly panel and web welded by the rail-type automatic welding equipment are shown in Figure 40. In Figure 40a, the panel includes a total of five welding layers and seven welding passes. In Figure 40b, the web includes a total of three welding layers and four welding passes. The processed plate has clear passes without defects.

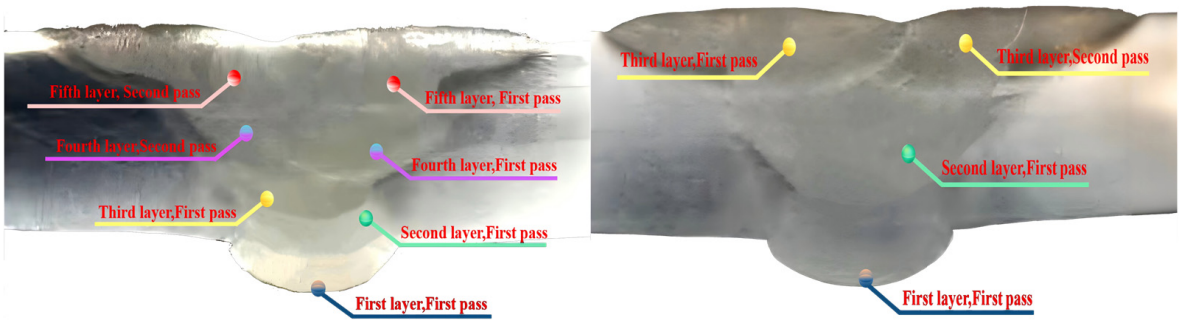

(**a**) (**b**)

Figure 40. Automatic welding equipment welding process renderings. (**a**) Panel multi-layer and multi-pass welding process effect. (**b**) Web multi-layer and multi-pass welding process effect.

6. Discussion

As shown in Figure 41, a comprehensive evaluation and analysis of the track-based automatic welding equipment for small assembly plates is conducted. Summarizing the analysis, this equipment has played a role in reducing costs and increasing efficiency in terms of practicality, specifically by reducing cost waste, shortening construction periods, and stabilizing processing quality. In terms of optimizability, future work can be based on this experimental method to verify and develop new applicable algorithms, working systems, and more intelligent and flexible robotic arms. Furthermore, the development of multiple robotic arms operating simultaneously on the track can be considered, and through structural optimization, the equipment can be designed with a lightweight focus, increasing productivity while enhancing equipment performance and extending service life, thereby further improving economic benefits. In terms of flexible adaptability, the equipment can adapt to various work scenarios by adjusting the installation height. After installation and commissioning without manual handling, it can complete automated continuous batch processing. According to the development trend in the field of automatic welding, this equipment can further be custom-developed to include multi-weld type recognition and tracking methods [31–33], automatic welding data models [34], real-time control systems, and processing algorithms [35–37]. In terms of value, this paper provides a certain reference significance for theoretical analysis and practical application in the subsequent research and development of track-based automatic welding equipment.

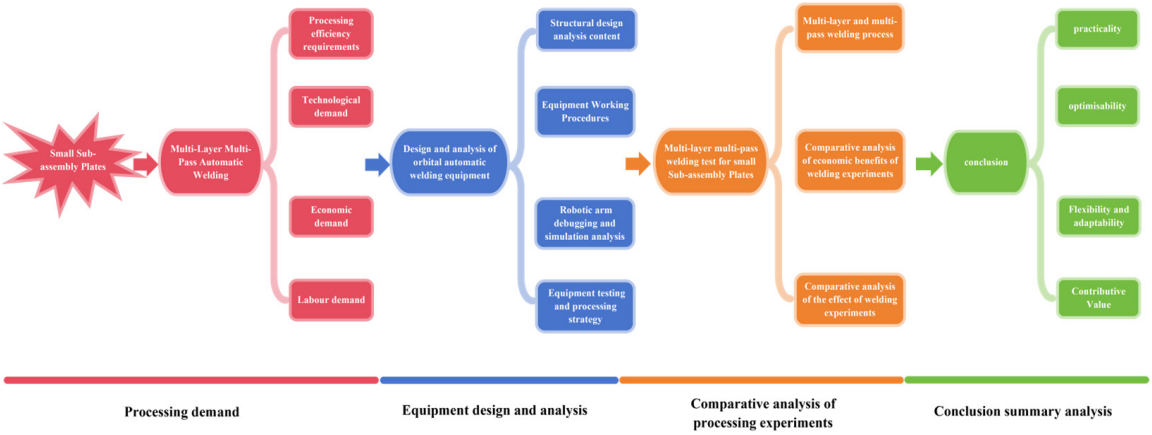

Figure 41. Comprehensive evaluation diagram.

7. Conclusions

This equipment eliminates the need for manual repetitive handling and enables rapid equipment assembly. Based on rail operation, it offers a flexible working range, realizing smooth, efficient, and continuous batch automatic welding in confined spaces. Additionally, the equipment can be connected to external power sources and numerical control operation boxes, supporting offline operations and function customization. The equipped teach pendant includes remote control, start, and emergency stop functions. Using this paper as an example, the following is a comparative analysis of other automatic welding solutions in terms of processing accuracy, efficiency, and cost. Reference [9] utilized automatic welding equipment, achieving a final welding formation rate of 85%. Through single-layer welding, the processing efficiency reached 600–800 plates per hour, enhancing the processing speed for simple welding of small structural parts. However, compared with this paper, that study requires manual handling and fixing of workpieces, which introduces certain errors and results in some waste in labor and material processing costs. Improvements are needed when dealing with slightly more complex welding processes and workpiece tasks. Reference [5] completed the design of a six-DOF gantry welding robot. However, compared with this paper, the track mechanical structure adopted in that design can be further refined and improved to better align with actual working conditions, thereby ensuring processing efficiency and accuracy during equipment operation and processing. In reference [11], plates with specifications of 200 × 150 × 10 mm were processed, with an average welding speed of 0.6–0.8 meters per hour. The weld seams were uniform with good quality. However, compared with this paper, their continuous batch processing of small plates could further optimize processing speed and efficiency while maintaining the current processing quality. Reference [12] completed the design of automatic pipe welding equipment, achieving good weld appearance and satisfactory welding speed. However, compared with this paper, further considerations can be made in integrated equipment selection and mechanical structure design to expand the specifications of processable pipes and enhance the precision of automatic welding.

Focusing on typical application cases and design research of multi-layer multi-pass welding equipment for small assembled plates, this paper addresses, to some extent, the low automation level in processing small assembled plates in the shipbuilding industry, which heavily relies on traditional manual processing. Compared with other automatic welding solutions, this scheme avoids repetitive manual handling of equipment and intervention operations. Through rapid installation and commissioning based on rails, continuous batch welding of small assembled plates can be carried out without additional operations once the setup is completed. Compared with other automated application schemes, this paper demonstrates certain advantages in processing accuracy, efficiency, and cost when handling plates of different batches and specifications.

In the future, integrated equipment such as robotic arms can be selected and developed according to technical requirements to meet different levels of processing and adapt to different working conditions. From the perspective of future development directions and potential industrial application environments, the end flange, mechanical structure, sensing and control systems, power supply, and other integrated components of this equipment can be flexibly selected and expanded to more application scenarios and technical fields, such as grinding, handling, and spraying.

Finally, combined with Figure 42, the following three points are summarized and organized.

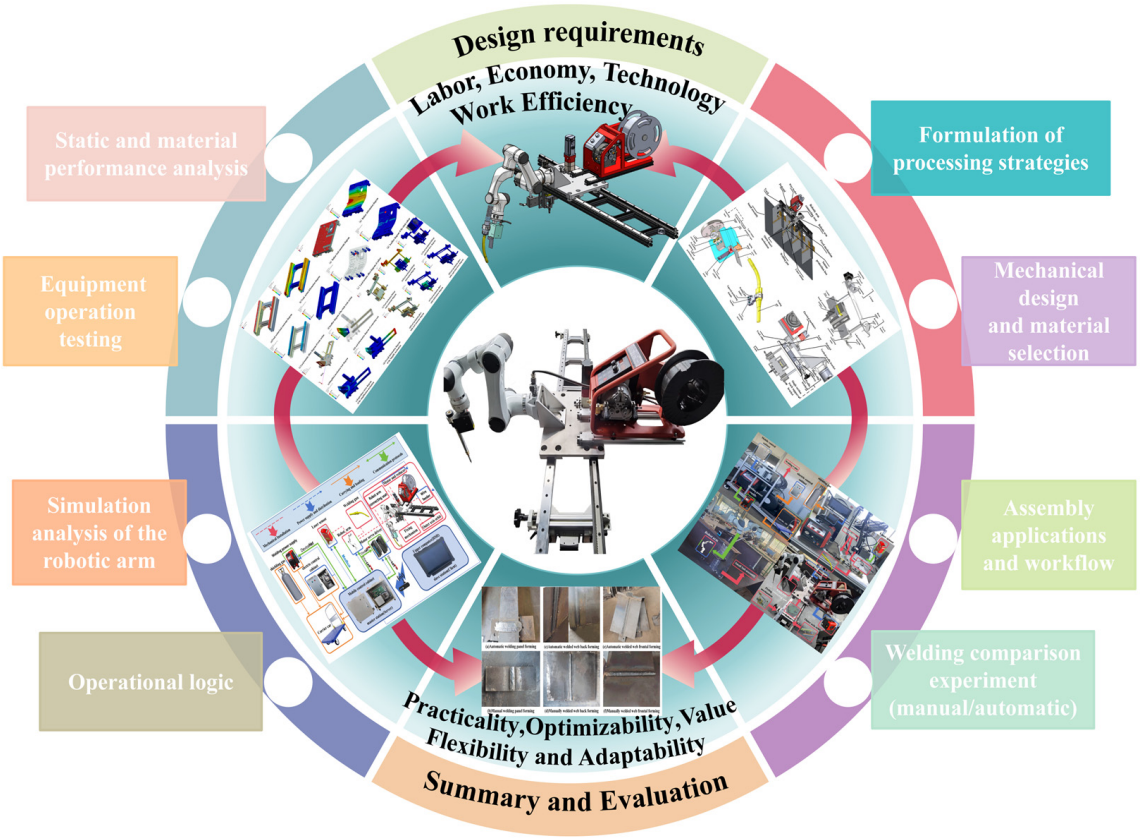

Figure 42. Summary diagram.

(1) This article completes the development of the rail-type multi-layer and multi-pass welding equipment through the analysis of sub-assembly plate processing requirements, equipment design, comparative processing experiments, and conclusion summaries. It organizes the equipment's working logic and workflow and summarizes the mechanical design and static analysis methods of the equipment structure, robotic arm debugging methods, research on spatial coordinate transformation methods in robotic arm simulation analysis, robotic arm kinematics analysis and solutions, posture verification, and quantitative and non-quantitative workspace analysis methods.

(2) The study includes equipment operation testing, analysis of group-assembled working conditions in processing strategies, and visual scanning processing of plate bevels.

(3) The technical parameters and experimental process flow of the multi-layer and multi-pass welding process for group-assembled plates were developed and validated. Comparative experimental analysis of welding effects and benefits revealed that single plates, bevel plates with different gaps, and large batches of uniformly specified plates in group-assembled plates all achieved certain degrees of savings in consumable costs and time costs, thereby improving economic benefits compared to manual welding.

Author Contributions: Conceptualization, Y.C. and G.Y.; methodology, Y.C.; software, Y.C.; validation, G.Y., J.Y., and Y.J.; formal analysis, Y.C. and Y.J.; investigation, G.Y. and J.Y.; resources, Y.C. and G.Y.; data curation, Y.C. and Y.J.; writing—original draft preparation, Y.C.; writing—review and editing, Y.C.; visualization, J.Y.; supervision, G.Y. and J.Y.; project administration, G.Y. and Y.C.; funding acquisition, G.Y. All authors have read and agreed to the published version of the manuscript.

Funding: This research was supported by CSSC Digital Information Technology Co., Ltd., grant number ZWZ202407M06.

Institutional Review Board Statement: Not applicable.

Informed Consent Statement: Informed consent was obtained from all subjects involved in the study.

Data Availability Statement: The original contributions presented in the study are included in the article, further inquiries can be directed to the corresponding author.

Acknowledgments: The authors would like to express their gratitude to Wang Feng and his companies, Youte Machinery Tools (Dalian) Co., Ltd., and Vivid Robotics (Dalian) Co., Ltd., for their assistance during the experiments.

Conflicts of Interest: The authors declare that this study received funding from CSSC Digital Information Technology Co., Ltd. The funder was not involved in the study design, collection, analysis, interpretation of data, the writing of this article or the decision to submit it for publication.

Appendix A

The detailed technical parameters in the visual scanning strategy of the automatic welding equipment in this paper are provided here.

Serial Number	World Coordinates (mm)	External Axis Position (U/mm)	Articular Angle J1~J6 (°)
0	(712.23, −81.79, 370.02)	−93.689	(0°, −120°, 120°, −180°, 90°, 0°)
1	(−138.03, −81.82, 411.05)	−93.689	(0°, −120°, 100°, −180°, −105°, 0°)
2	(−138.07, −81.82, 411.02)	349.877	(0°, −120°, 100°, −180°, −105°, 0°)
3	(−138.06, −81.85, 411.02)	59.883	(0°, −120°, 100°, −180°, −105°, 0°)
4	(−315.64, −81.82, 489.02)	59.883	(0°, −90°, 108°, −180°, −75°, 0°)
5	(−350.32, −81.82, 494.72)	59.883	(0°, −85°, 110°, −180°, −68°, 0°)
6	(−364.79, 123.12, 447.57)	59.883	(−110°, −98°, 90°, −223°, −100°, 0°)
7	(−341.63, 301.42, 455.65)	−35.729	(−150°, −118°, 96°, −250°, −95°, −135°)
8	(−450.1, 300, 501.08)	−35.729	(−156°, −95°, 58°, −258°, −98°, −150°)
9	(−114.91, 300, 501.08)	−35.729	(−130°, −108°, 111°, −221°, −88°, −113°)
10	(−215.34, −81.87, 530.19)	−35.729	(0°, −90°, 90°, −180°, −90°, 0°)
11	(−115.89, 100, 421.11)	354.268	(21°, −90°, 67°, −157°, −111°, 77°)
12	(−123.76, −155.15, 485.91)	336.317	(−16°, −92°, 72°, −197°, −101°, 59°)
13	(712.23, −81.79, 370.17)	−35.729	(0°, −120°, 120°, −180°, 90°, 0°)

References

1. Wang, B.; Hu, S.J.; Sun, L.; Freiheit, T. Intelligent Welding System Technologies: State-of-the-Art Review and Perspectives. *J. Manuf. Syst.* **2020**, *56*, 373–391. [CrossRef]
2. Samson, R.M.; Aravind, R.; Muthiya, S.J.; Dhanraj, J.A.; Velmurugan, K.; Oo, S.L. Microfriction Stir Welding of Aluminium Using ABB IRB 1410 Robot. *Adv. Mater. Sci. Eng.* **2023**, *2023*, 8033881. [CrossRef]
3. Lee, D.; Ku, N.; Kim, T.-W.; Kim, J.; Lee, K.-Y.; Son, Y.-S. Development and Application of an Intelligent Welding Robot System for Shipbuilding. *Rob. Comput. Integr. Manuf.* **2011**, *27*, 377–388. [CrossRef]
4. Dharmawan, A.G.; Vibhute, A.A.; Foong, S.; Soh, G.S.; Otto, K. A Survey of Platform Designs for Portable Robotic Welding in Large Scale Structures. In Proceedings of the 2014 13th International Conference on Control Automation Robotics & Vision (ICARCV), Singapore, 10–12 December 2014; IEEE: Piscataway, NJ, USA, 2014; pp. 1683–1688.
5. Saleem, M.; Jameel, S.; Hassan, A.; Khan, Z.H. Design and Fabrication of a Six DOF Gantry Robot for Welding Applications. In Proceedings of the 2024 ASU International Conference in Emerging Technologies for Sustainability and Intelligent Systems (ICETSIS), Manama, Bahrain, 28–29 January 2024; IEEE: Piscataway, NJ, USA, 2024; pp. 1940–1946.
6. Yi, J.; Qingqing, H.; Zhaoen, D.; Chao, Z.; Jianfeng, Y.; Chunjian, H. Structural Design and Kinematic Analysis of a Welding Robot for Liquefied Natural Gas Membrane Tank Automatic Welding. *Int. J. Adv. Manuf. Technol.* **2022**, *122*, 461–474. [CrossRef]
7. Kermorgant, O. A Magnetic Climbing Robot to Perform Autonomous Welding in the Shipbuilding Industry. *Rob. Comput. Integr. Manuf.* **2018**, *53*, 178–186. [CrossRef]
8. Yu, S.; Guan, Y.; Yang, Z.; Liu, C.; Hu, J.; Hong, J.; Zhu, H.; Zhang, T. Multiseam Tracking with a Portable Robotic Welding System in Unstructured Environments. *Int. J. Adv. Manuf. Technol.* **2022**, *122*, 2077–2094. [CrossRef]

9. Ren, Y.; Guo, W.; Wang, X.; Hu, C.; Wang, L.; He, X.; Xing, J. Design and Test of Duckbill Welding Robot for Cotton Seeder. *Agriculture* **2022**, *13*, 31. [CrossRef]
10. Park, J.-H.; Moon, H.-S. Advanced Automatic Welding System for Offshore Pipeline System with Seam Tracking Function. *Appl. Sci.* **2020**, *10*, 324. [CrossRef]
11. Wu, Y.; Zhu, Y.; Chen, X.; Wan, S. Automatic Welding of Corrugated Steel Webs on Composite Box Girder with Corrugated Steel Webs. *Adv. Civ. Eng.* **2024**, *2024*, 5289340. [CrossRef]
12. Zhou, L.; Guo, Y.; Yin, T.; Wang, X.; Ma, Z.; Wang, H. Application of Rail-Type Welding Robot in Automatic Welding of Pipeline. *J. Phys. Conf. Ser.* **2023**, *2437*, 012118. [CrossRef]
13. Reis, M.; Şerifağaoğlu, E. A Smart Handheld Welding Torch Device for Manual Spot Laser Welding. *Appl. Sci.* **2022**, *12*, 11137. [CrossRef]
14. Natesan, N.; Jegadeeshwaran, R.; Sakthivel, G.; Arunkumar, V. Design and Analysis of Robot and Fixture Pedestal for OTC FD-V8 MAG Welding Robot. *J. Phys. Conf. Ser.* **2023**, *2601*, 012008. [CrossRef]
15. Guo, J.; Zhu, Z.; Sun, B.; Zhang, T. A Novel Field Box Girder Welding Robot and Realization of All-Position Welding Process Based on Visual Servoing. *J. Manuf. Process.* **2021**, *63*, 70–79. [CrossRef]
16. Chou, C.-C.; Yu, G.-J.; Wang, K.-J.; Chang, W.-T.; Wu, C.-L.; Zhao, C.C.-J.; Yang, C.-Y.; Chou, M.-T. Application of Robotic Welding Technology to the Continuity Plate Weld within a Steel Built-up Box Column in Buildings. *Int. J. Precis. Eng. Manuf.* **2023**, *24*, 1563–1576. [CrossRef]
17. Seth, A.; Kuruvilla, J.K.; Sharma, S.; Duttagupta, J.; Jaiswal, A. Design and Simulation of 6-DOF Cylindrical Robotic Manipulator Using Finite Element Analysis. *Mater. Today Proc.* **2022**, *62*, 1521–1525. [CrossRef]
18. Li, X.; Shao, H.; Li, G.; Liu, W.; Liu, C. Static Simulation and Structure Optimization of Key Parts of Joint Welding Robots. In Proceedings of the 2018 IEEE International Conference on Mechatronics and Automation (ICMA), Changchun, China, 5–8 August 2018; IEEE: Piscataway, NJ, USA, 2018; pp. 282–287.
19. Xu, F.; Xu, Y.; Zhang, H.; Chen, S. Application of Sensing Technology in Intelligent Robotic Arc Welding: A Review. *J. Manuf. Process.* **2022**, *79*, 854–880. [CrossRef]
20. Lei, T.; Rong, Y.; Wang, H.; Huang, Y.; Li, M. A Review of Vision-Aided Robotic Welding. *Comput. Ind.* **2020**, *123*, 103326. [CrossRef]
21. Guo, Q.; Yang, Z.; Xu, J.; Jiang, Y.; Wang, W.; Liu, Z.; Zhao, W.; Sun, Y. Progress, Challenges and Trends on Vision Sensing Technologies in Automatic/Intelligent Robotic Welding: State-of-the-Art Review. *Rob. Comput. Integr. Manuf.* **2024**, *89*, 102767. [CrossRef]
22. Zhang, Q.; Xiao, R.; Liu, Z.; Duan, J.; Qin, J. Process Simulation and Optimization of Arc Welding Robot Workstation Based on Digital Twin. *Machines* **2023**, *11*, 53. [CrossRef]
23. Luo, H.; Fu, J.; Jiao, L.; Liu, G.; Yu, C.; Wu, T. Kinematics and Dynamics Analysis of a New-Type Friction Stir Welding Robot and Its Simulation. *Adv. Mech. Eng.* **2019**, *11*, 168781401986651. [CrossRef]
24. Fang, H.C.; Ong, S.K.; Nee, A.Y.C. Adaptive Pass Planning and Optimization for Robotic Welding of Complex Joints. *Adv. Manuf.* **2017**, *5*, 93–104. [CrossRef]
25. Wang, X.; Zhou, X.; Xia, Z.; Gu, X. A Survey of Welding Robot Intelligent Path Optimization. *J. Manuf. Process.* **2021**, *63*, 14–23. [CrossRef]
26. Zhang, G.; Zhang, Y.; Tuo, S.; Hou, Z.; Yang, W.; Xu, Z.; Wu, Y.; Yuan, H.; Shin, K. A Novel Seam Tracking Technique with a Four-Step Method and Experimental Investigation of Robotic Welding Oriented to Complex Welding Seam. *Sensors* **2021**, *21*, 3067. [CrossRef] [PubMed]
27. Fang, H.; Ong, S.; Nee, A. Robot Path Planning Optimization for Welding Complex Joints. *Int. J. Adv. Manuf. Technol.* **2017**, *90*, 3829–3839. [CrossRef]
28. Zhang, K.; Yan, M.; Huang, T.; Zheng, J.; Li, Z. 3D Reconstruction of Complex Spatial Weld Seam for Autonomous Welding by Laser Structured Light Scanning. *J. Manuf. Process.* **2019**, *39*, 200–207. [CrossRef]
29. Rao, M.; Liu, K.; Sheng, Z.; Xiao, R.; Yang, X.; Zhang, W.; Zhong, Z.; Lu, Y.; Chen, H. A Novel Filling Strategy for Robotic Multi-Layer and Multi-Pass Welding Based on Point Clouds for Saddle-Shaped Weld Seams. *J. Manuf. Process.* **2024**, *121*, 233–245. [CrossRef]
30. Han, C.; Yang, C.; Kim, H.; Park, S. The Effects of Robot Welding and Manual Welding on the Low- and High-Cycle Fatigue Lives of SM50A Carbon Steel Weld Zones. *Adv. Mech. Eng.* **2019**, *11*, 1687814019828266. [CrossRef]
31. Rout, A.; Deepak, B.B.V.L.; Biswal, B.B. Advances in Weld Seam Tracking Techniques for Robotic Welding: A Review. *Rob. Comput. Integr. Manuf.* **2019**, *56*, 12–37. [CrossRef]
32. Shah, H.N.M.; Sulaiman, M.; Shukor, A.Z.; Kamis, Z.; Rahman, A.A. Butt Welding Joints Recognition and Location Identification by Using Local Thresholding. *Rob. Comput. Integr. Manuf.* **2018**, *51*, 181–188. [CrossRef]
33. Xue, K.; Wang, Z.; Shen, J.; Hu, S.; Zhen, Y.; Liu, J.; Wu, D.; Yang, H. Robotic Seam Tracking System Based on Vision Sensing and Human-Machine Interaction for Multi-Pass MAG Welding. *J. Manuf. Process.* **2021**, *63*, 48–59. [CrossRef]
34. Shen, W.; Hu, T.; Zhang, C.; Ye, Y.; Li, Z. A Welding Task Data Model for Intelligent Process Planning of Robotic Welding. *Robot. Comput.-Integr. Manuf.* **2020**, *64*, 101934. [CrossRef]
35. Du, R.; Xu, Y.; Hou, Z.; Shu, J.; Chen, S. Strong Noise Image Processing for Vision-Based Seam Tracking in Robotic Gas Metal Arc Welding. *Int. J. Adv. Manuf. Technol.* **2019**, *101*, 2135–2149. [CrossRef]

36. Zou, Y.; Wang, Y.; Zhou, W.; Chen, X. Real-Time Seam Tracking Control System Based on Line Laser Visions. *Opt. Laser Technol.* **2018**, *103*, 182–192. [CrossRef]
37. Tung, P.C.; Wu, M.C.; Hwang, Y.R. An image-guided mobile robotic welding system for SMAW repair processes. *Int. J. Mach. Tools Manuf.* **2004**, *44*, 1223–1233. [CrossRef]